A Level-Set/FEM approach for particle bed growth in Stokes–Darcy suspension filtration

Ayoub Badia, Nicolas Moulin, Renaud Ferrier, Cédric Descamps, Sylvain Drapier

A Level-Set/FEM approach for particle bed growth in Stokes–Darcy suspension filtration

Ayoub Badia[a,*], Nicolas Moulin[a], Renaud Ferrier[a], Cédric Descamps[b], Sylvain Drapier[a]

[a]*Mines Saint-Étienne, Université de Lyon, CNRS & UMR 5307 LGF, Centre SMS, Saint-Étienne, 42100, France*
[b]*Safran Ceramics, a technology platform of Safran Tech, 105 avenue Marcel Dassault, Mérignac, 33700 , France*

Abstract

This article presents an innovative approach to modeling particle bed growth through suspension dead-end filtration, a process of paramount importance in various industrial and environmental contexts. More precisely, it focuses on the numerical formulation of a continuous approach based on a Stokes–Darcy coupling. In a Level-set/FEM frame, this model effectively captures the dynamic evolution of particle beds (cake), taking into account the interaction between suspended particles and porous media. Model validation is also a key focus of this paper. Numerical tests are carried out under various conditions, and their results are compared with analytical solutions and experimental data drawn from the literature. This permits corroboration of the predictive capabilities of the model, confirming the robustness and accuracy of the proposed approach. Firstly, Stokes–Darcy coupled flows are investigated in simplified cases such as rectangular geometries and coaxial cylinders. These scenarios serve as benchmarks to assess the model performance under simple and varied conditions. Additionally, the more challenging case of a three-dimensional anisotropic flow between two ellipsoids is addressed, where the evolution of the cake takes place in three dimensions. Through rigorous analysis and comparison with analytical solutions, the model is proved efficient in capturing the inherent complexities of such scenarios. Finally, richer two-dimensional Stokes–Darcy flows are considered, in the presence of both impermeable and permeable obstacles, representing a crucial step towards modeling real industrial processes. This last study highlights not only the formation of particle-free zones but also the practical relevance of this work.

Keywords: Stokes–Darcy coupling, Suspension filtration, FEM, Level-Set, Particle bed growth, Mass transfer

1. Introduction

The formation of particle beds through suspension dead-end filtration is a widely used method in various industrial applications, such as the manufacturing processes of food, pharmaceutical or composite materials. In this method, particles transported in a controlled flow first deposit on

*Corresponding author
Email address: ayoub.badia@cea.fr (Ayoub Badia)

a filtrating membrane, and then continue to deposit on the so-called porous filter cake growing under the continuous deposition. Controlling this growth is of the utmost importance since it will determine the final geometry and properties of the particle cake. In specific industrial applications, such as the production of ceramic matrix composites (CMC), this process also known as "slurry cast process", is used to optimize the densification phase (matrix injection into a fibrous structure [1]), enhancing the material quality. Figure 1, extracted from [2], illustrates a CMC cross-section after the slurry cast process. It can notably be seen that the filling of the fibrous structure by the suspension has not been optimal, with several zones (macropores) remaining incompletely filled by the particles. Understanding and modeling the formation of particle beds are therefore essential for optimizing this type of processes.

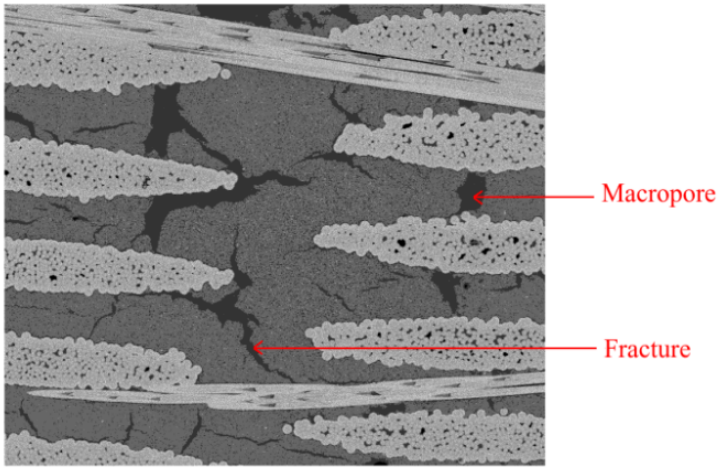

Figure 1: SEM imaging of a cross-section of CMC material after the slurry cast process. Image extracted from [2].

Since the seminal work of Ruth *et al.* [3, 4, 5], numerous theoretical studies have been provided to better describe the formation of a filter cake, and hence understand both filtration and sedimentation of a suspension. Ruth's work, built on the cake seen as a resistance in the sense of Ohm's law, has led to several subsequent studies, commonly referred to in the literature as the "conventional theory" [6, 7, 8, 9, 10, 11, 12, 13, 14, 15]. Many of these theoretical works require the evaluation of the cake permeability, *i.e.* the inverse of its resistance. For example, Belfort *et al.* [16] and Chew *et al.* [17] determine, respectively analytically and experimentally, the filter cake temporal evolution relying on the well-known Kozeny-Carman's equation [18]. However, such simple permeability models exhibit some limitations in certain cases, leading to the introduction of alternative expressions encompassing more of the local fluid-structure interactions that build up permeability at upper scales; see the review [19] or dedicated literature in composite manufacturing such as [20] for example. Alternatively, some studies propose to model filtration as a diffusion process, yielding a diffusion-like filtration equation [21, 22, 23, 24]. However, this type of model is not very popular and remains subject to debate [25, 26]. Other filtration models can also be mentioned, such as those based on multiphase theory [27, 28, 29] or the phenomenological approach [30, 31]. For more details, we refer the reader to the reviews by Lee *et al.* [32] or Olivier *et al.* [19], where the authors carry out a comparative analysis of various models and approaches,

aiming to highlight their specific similarities and differences. While these filtration models may perform adequately in simple or 1D configurations, they are limited in complex 3D scenarios. In the present paper, we endeavor to introduce a 3D numerical model that aims at simulating cake formation in complex scenarios representative of industrial cases.

In the same vein, numerical modeling of the suspension filtration has been developed considerably, particularly with the discrete element method (DEM) [33, 34, 35, 36]. This method, based on a Lagrangian approach, describes the motion of each particle within a system, incorporating liquid phase considerations through liquid–particle interaction forces. More recently, several studies have proposed more accurate methods using an Eulerian–Lagrangian approach, coupling the DEM to describe particle motion with a computational fluid dynamics (CFD) method to describe the liquid flow [37, 38, 39, 40]. While the DEM provides convenient access to specific particle scale information, individual tracking of each particle can prove costly for large systems, such as those encountered in industrial applications.

Few works in the literature rely exclusively on CFD modeling for the evolution of filter cakes, with two physics separated by a moving interface to be represented. In [2] addressing dead-end filtration, the cake/suspension interface is determined using the particle concentration profile established by solving a convection–diffusion equation, which is not ideally suited for describing the complex typologies encountered in this kind of problem. Another notable work is [41] addressing particle deposition where a front-capturing method is employed, better suited for describing complex interfaces. However, this work does not address dead-end filtration but instead focuses on particle deposition issues, modelled in the article as a first-order reaction. Both studies are based on resolution using a finite volume method. When the interface is defined, two common approaches can be considered to couple free flow/porous medium systems [42, 43]. In the one-domain approach, both zones are represented within a single computational domain, considering the entire domain as a unified continuum. The well established Darcy-Brinkman's model implicitly describes the interface between free flow and porous medium through spatial variations in material parameters. In contrast, the two-domain approach represents free flow and porous medium flow as separate domains within the computational domain. Each domain has its own governing equations, with the free flow region described by Navier-Stokes equations and the porous medium region ruled by Darcy/Brinkman/Forchheimer laws, coupled through appropriate interface conditions.

In this context, the present paper proposes a different approach for the numerical simulation of particle accumulation in dead-end filtration of a suspension, implementing CFD modeling based on the finite element method (FEM). This numerical method is better designed for complex interfaces where specific conditions need to be prescribed and, furthermore, advancements in fluid-porous medium coupling resolution are more established with this approach. The aim of the present study is to numerically model the spatial and temporal evolution of a particle bed with complex topology, considering the particle mass conservation which requires an explicit description of the free flow/porous medium interface. The two-domain approach is deemed more appropriate for this task. Furthermore, given the low Reynolds numbers typical of such problems, a Stokes–Darcy coupling is considered. The interface between these two media is represented by an Eulerian description (front-capturing) using the Level-Set (LS) method. Unlike methods relying on a Lagrangian description (front-tracking), front-capturing methods naturally take into account

topological changes, without requiring extensive remeshing and mesh adaptation [44]. The use of the Level-Set method in the numerical modeling of dead-end filtration offers a robust approach for representing the change in filter cake topology due to particle accumulation, and thus to accurately describe mass transfers from the fluid zone to the porous zone. This approach provides a detailed description of the filter cake evolution within a more reasonable computational time compared to discrete simulations.

This article is organized as follows. Section 2 deals with the mathematical modeling of the problem. The description of the problem is presented and the governing equations are exposed. The numerical implementation using the stabilized finite element method is presented in Section 3. In Section 4, the proposed numerical model is validated and the results obtained are discussed. Section 5 gives a brief conclusion of the proposed approach.

2. Mathematical modeling

2.1. Problem description

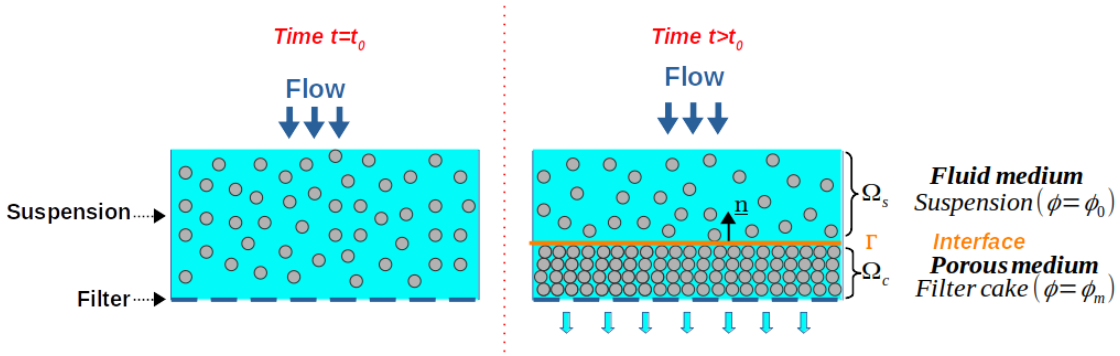

Figure 2: Schematic diagram of dead-end filtration of a solid particle suspension.

The problem considered here consists in modeling the filling process of a workpiece with particles, also known as *slurry cast process*. The objective is to model and simulate a dead-end filtration scenario applied to a uniform suspension of spherical solid particles (Figure2). A uniform suspension with a concentration $\phi = \phi_0$ (ϕ is the volume fraction of particles in the suspension) is continuously injected into a device containing a membrane filter at its outlet. This membrane filter is permeable to the fluid and impermeable to the particles. The particles transported in this prescribed flow first deposit on the filter membrane, and then keep on depositing afterwards on the so-called porous filter cake, which grows under the continuous deposition. Two distinct time-varying regions of interest can then be distinguished (Figure2): the first is a fluid region Ω_s, describing the uniform suspension with concentration $\phi = \phi_0$, while the second is a porous region Ω_c, characterizing the particles deposition (filter cake) with a jamming concentration $\phi = \phi_m$. The interface between both media, denoted as Γ, changes over time at velocity $\underline{v}_\Gamma$ and in the direction opposite to the flow.

2.2. Governing equations

From a continuous modeling point of view, it is necessary to describe a Stokes–Darcy flow, but with two porous domains involved for the region governed by the Darcy's equations: the first one being static (membrane filter), and the second one evolving over time (growing cake).

In the fluid region Ω_s, the considered suspension has a low particle concentration ($\phi < 0.2$). The flow is characterized by a low Reynolds number, and the migration of particles within the flow is assumed to be negligible. The particle concentration in region Ω_s therefore remains constant and uniform throughout the flow. In this case, the particle velocity is assumed to be equivalent to the fluid velocity ($\underline{v}^p = \underline{v}^f$, with $\underline{v}^f$ the fluid velocity and $\underline{v}^p$ the particle velocity), and the suspension can therefore be considered as a Newtonian fluid, solved by the classical Stokes' equations. The viscosity of the medium is constant and depends on the initial suspension concentration ϕ_0. The region Ω_s is described by the following equations [45, 46]:

$$\underline{\nabla} \cdot \underline{v}^s(\underline{x}) = 0 \tag{1a}$$

$$-\underline{\nabla} \cdot \left[2\eta_s \underline{\underline{\dot{\epsilon}}}\left(\underline{v}^s(\underline{x})\right)\right] + \underline{\nabla} p^s(\underline{x}) = 0 \tag{1b}$$

where p^s denotes the suspension pressure, $\underline{v}^s$ the suspension velocity (particles and fluid have similar velocity $\underline{v}^p = \underline{v}^f = \underline{v}^s$) and $\underline{\underline{\dot{\epsilon}}}$ the strain rate tensor. η_s is the suspension viscosity, whose expression is given by [47, 48]:

$$\eta_s = \eta_f \left[1 + \frac{5\phi_0/4}{1 - \frac{\phi_0}{\phi_m}}\right]^2 \tag{2}$$

with η_f the suspending fluid viscosity, ϕ_0 the initial suspension concentration and ϕ_m the jamming concentration. The viscosity of the suspension increases with the presence of particles.

The Stokes equations (1) must be complemented with boundary conditions to close the problem which is defined in the domain $\Omega_s \in \mathbb{R}^{dim}$ (where the exponent *dim* corresponds to the problem dimension, $dim = 2$ or $dim = 3$). The domain boundary $\partial\Omega_s$ is decomposed into two distinct parts $\partial\Omega_s \setminus \Gamma = \partial\Omega_{s,D} \cup \partial\Omega_{s,N}$ with $\partial\Omega_{s,D} \cap \partial\Omega_{s,N} = \emptyset$, corresponding respectively to the regions where Dirichlet and Neumann boundary conditions are prescribed. Let us point out that this split is not a topological one, but is to be considered as an exclusive decomposition of the vectorial unknowns on this boundary $\partial\Omega_s$, component by component. The inner problem formulated in Ω_s (Eq. 1) is now closed thanks to these boundary conditions named *Type I*, that read:

$$\underline{v}^s = \underline{v} \qquad \text{on } \partial\Omega_{s,D} \tag{3a}$$

$$\underline{\underline{\sigma}}^s \cdot \underline{n}^s = -p_{ext,s}\, \underline{n}^s \qquad \text{on } \partial\Omega_{s,N} \tag{3b}$$

where $\underline{n}^s$ is the external normal vector to $\partial\Omega_s$ and $\underline{\underline{\sigma}}^s$ is the Cauchy stress tensor, defined by $\underline{\underline{\sigma}}^s = 2\eta_s \underline{\underline{\dot{\epsilon}}}(\underline{v}^s) - p^s \underline{\underline{I}}$. A second type of boundary conditions for Dirichlet, named *Type II*, can also be prescribed for this problem with tangential stress components and normal velocity defined; it

writes:

$$\underline{v}^s \cdot \underline{n} = v_s \qquad \text{on } \partial\Omega_{s,D} \tag{4a}$$

$$\underline{t} \cdot \underline{\underline{\sigma}}^c \cdot \underline{n} = \tau_{ext} \quad , \forall \text{ t tangent to } \partial\Omega_{s,D} \qquad \text{on } \partial\Omega_{s,D} \tag{4b}$$

$$\underline{\underline{\sigma}}^s \cdot \underline{n}^s = -p_{ext,s}\underline{n}^s \qquad \text{on } \partial\Omega_{s,N} \tag{4c}$$

Conditions (4a) and (4b) will be used typically for impervious wall conditions.

The filter cake region Ω_c can be represented as an equivalent porous medium. Both the filter membrane and the filter cake are modelled using Darcy's approach, with different permeabilities constant over time, they are described by the following equations:

$$\underline{\nabla} \cdot \underline{v}^c(\underline{x}) = 0 \tag{5a}$$

$$\eta_f \underline{\underline{K}}^{-1} \underline{v}^c(\underline{x}) + \underline{\nabla} p^c(\underline{x}) = 0 \tag{5b}$$

where $\underline{v}^c$, p^c and η_f are respectively the velocity, pressure and viscosity of the interstitial fluid. $\underline{\underline{K}}$ denotes the porous medium permeability ($\underline{\underline{K}} = \underline{\underline{K}}^c$ for the filter cake and $\underline{\underline{K}} = \underline{\underline{K}}^f$ for the filter membrane). The permeability is denoted as K in the isotropic case. Like for Stokes, the Darcy's equations (5) defined in the domain $\Omega_c \in \mathbb{R}^{dim}$, are complemented with boundary conditions on $\partial\Omega_c \setminus \Gamma = \partial\Omega_{c,D} \cup \partial\Omega_{c,N}$ with $\partial\Omega_{c,D} \cap \partial\Omega_{c,N} = \emptyset$, and with v_c and $p_{ext,c}$ corresponding respectively to Dirichlet boundary condition for velocity, and Neumann boundary condition for pressure:

$$\underline{v}^c \cdot \underline{n} = v_c \qquad \text{on } \partial\Omega_{c,D} \tag{6a}$$

$$p^c = p_{ext,c} \qquad \text{on } \partial\Omega_{c,N} \tag{6b}$$

where $\underline{n}$ is the outward normal vector to $\partial\Omega_c$.

As the fluid flows from a free zone (Stokes) to a porous zone (Darcy), velocities and pressures must obey continuity conditions at the interface Γ between these zones, namely continuity of normal velocity, continuity of normal stress and Beavers–Joseph–Saffman condition [49, 50], described as follows:

$$\underline{v}^c \cdot \underline{n} = \underline{v}^s \cdot \underline{n} \tag{7a}$$

$$\underline{n} \cdot \underline{\underline{\sigma}}^c \cdot \underline{n} = \underline{n} \cdot \underline{\underline{\sigma}}^s \cdot \underline{n} \tag{7b}$$

$$2\underline{n} \cdot \underline{\underline{\dot{\epsilon}}}(\underline{v}^s) \cdot \underline{t} = \frac{-\alpha}{\sqrt{K}} \underline{v}^s \cdot \underline{t} \tag{7c}$$

where $\underline{\underline{\sigma}}^c$ is the porous medium stress, equal to the Darcy fluid pressure ($\underline{\underline{\sigma}}^c = -p^c \underline{\underline{I}}$), α is the slip coefficient and $\underline{t}$ are the vectors tangent to the interface.

The Beavers–Joseph–Saffman condition (7c) specifies the tangential velocity on the interface Γ. Various options exist in literature for the coupling conditions on the tangential velocity component [51], with the most commonly used being the Beavers–Joseph (BJ) and Beavers–Joseph–Saffman (BJS) conditions. In the case of forced fluid infiltration into a porous medium, where the flow is primarily perpendicular to the porous bed and the tangential component is negligible, Eggenweiler [52] shows that the BJS condition reduces approximately to the no-slip condition

$\underline{v}^s \cdot \underline{t} = 0$ and provides consistent results. Additionally, in a close configuration with further specific boundary conditions Carraro *et al.* [53] prescribe a no-slip condition for the tangential velocity.

Furthermore, both BJ and BJS conditions are subject to debate, and research is ongoing to improve them. Indeed, [54] demonstrate that these conditions, originally proposed for flows parallel to the porous layer, are not suitable for arbitrary flow directions. In our present problem, the flow is mainly perpendicular to the interface. To avoid non-physical repercussions from using a BJS condition, such as influences on interface topology or mass loss, a no-slip condition will be preferred. Condition (7c) is thus replaced by $\underline{v}^s \cdot \underline{t} = 0$.

The interface Γ separating the fluid and porous zones is expected to evolve over time. This evolution depends on the suspension mass balance flowing across the moving cake boundary. To capture and locate this interface, we employ the Level-Set method [55]. This method uses a function $\Phi(\underline{x}, t)$ corresponding most often to the signed distance to the interface. This function is positive if point $\underline{x}$ lies inside Ω_s, negative if it lies outside Ω_s, and zero if it lies on the interface, defined by :

$$\Phi(\underline{x}, t = 0) = \begin{cases} \min\limits_{p \in \Gamma} \|\underline{x} - p\| & \text{if } \underline{x} \in \Omega_s \\ -\min\limits_{p \in \Gamma} \|\underline{x} - p\| & \text{if } \underline{x} \notin \Omega_s \end{cases} \tag{8}$$

To capture the interface in time, the Level-Set function $\Phi(\underline{x}, t)$ is advected using the classical transport equation with a velocity $\underline{v}_\Gamma$ derived from the physical problem:

$$\frac{\partial \Phi}{\partial t} + \underline{v}_\Gamma \cdot \underline{\nabla} \Phi = 0 \tag{9}$$

In our problem, it is important to note that the interface between the two zones is not directly transported by the fluid velocity like in fluid front propagation problems (for instance [56, 57, 44, 20]), but results from the accumulation of particles in the porous zone. Thus, the velocity $\underline{v}_\Gamma$ must be determined.

2.3. Determination of the interface velocity

In a suspension flow of solid spherical particles, the particle mass conservation reads [58]:

$$\frac{\partial \phi \rho^p}{\partial t} + \underline{\nabla} \cdot (\phi \rho^p \underline{v}^p) = 0 \qquad , \forall \underline{x} \in \Omega_s \cup \Omega_c \tag{10}$$

where ϕ, ρ^p and $\underline{v}^p$ denote, respectively, the concentration, density, and velocity of the particles.

The study domain here contains a discontinuity dividing it into two continuous sub-domains, Ω_s and Ω_c, separated by the interface Γ. The above equation (Eq.(10)) can only be applied within each sub-domain; it is not valid on the interface where there may be strong variations. A condition on Γ is then necessary to describe the mass transfer between the two sub-domains and thus the mass conservation throughout the entire domain. Rewriting the integral mass balance to include both media and the mobile interface implies the following jump condition on Γ:

$$[\![\phi \rho^p (\underline{v}^p - \underline{v}_\Gamma)]\!] \cdot \underline{n} = 0 \tag{11}$$

where $\underline{v}_\Gamma$ is the interface velocity. $[\![f]\!] = f_s - f_c$ represents the jump in quantity f with f_s and f_c the values of f in Ω_s and Ω_c respectively. $\underline{n}$ is the external normal vector to Ω_c. The particle density does not vary independently on the domain where they are present, Ω_s or Ω_c, so one can then write $\rho_c^p = \rho_s^p$. The jump relation (11) yields the interface velocity $\underline{v}_\Gamma$, i.e. the Level-Set velocity:

$$\underline{v}_\Gamma \cdot \underline{n} = \left(\frac{\phi_c \underline{v}_c^p - \phi_s \underline{v}_s^p}{\phi_c - \phi_s} \right) \cdot \underline{n} \tag{12}$$

In the porous zone Ω_c, particles are immobile and the concentration is the jamming concentration, i.e. $\underline{v}_c^p = 0$ and $\phi_c = \phi_m$. In the fluid zone Ω_s, the concentration is constant $\phi_s = \phi_0$ and particles flow at the same velocity as the fluid, determined by Stokes' equations, i.e. $\underline{v}_s^p = \underline{v}^s$. Consequently, the Level-Set velocity is derived as follows:

$$\underline{v}_\Gamma \cdot \underline{n} = -\frac{\phi_0}{\phi_m - \phi_0} \underline{v}^s \cdot \underline{n} \tag{13}$$

We can notice that since ϕ_m and ϕ_0 are known constants, the Level-Set velocity is negatively proportional to the suspension velocity, calculated with the Stokes' equations. A summary of the problem modeling is given in Figure3.

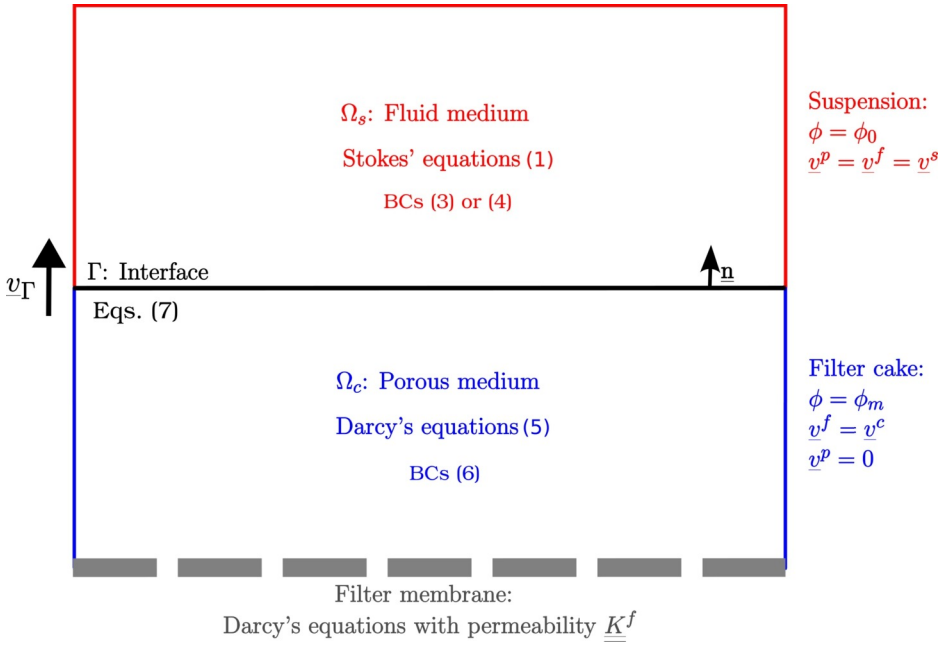

Figure 3: Problem modeling synthesis.

3. Numerical implementation

With the physical flow models established, the corresponding numerical implementation is now presented. This numerical resolution is carried out in the Zset [1] (development version) environment [59]. Numerous references are available in the literature concerning the resolution of

[1] http://www.zset-software.com/

Stokes–Darcy/Level-Set problems, in particular [60, 56, 61, 62]. This section is based on these works.

The Stokes and Darcy problems must be coupled using the continuity conditions described above (Eq.(7)). The coupling method, which can be direct or decoupled ([63, 64]), relies on interfaces that can be represented either explicitly by coincident meshes of these interfaces [65, 66] which may require remeshing operations, or implicitly by depicting the interface – mesh intersection. The latter solution has been chosen here, coupled with a monolithic approach of Stokes and Darcy flows using the same mesh.

The numerical resolution of the problem considered will be carried out using stabilized finite element formulations. We will consider the mixed velocity/pressure formulations stabilized by a variational multi-scale method, here the so-called Algebraic SubGrid Scale (ASGS) method [60].

In a monolithic approach, the difficulty is to formulate mathematically stable finite element solutions for both Stokes and Darcy flows. The various physical flow zones are then identified by the Level-Set function, obtained by a finite element resolution of the convection equation (9).

3.1. Integral weak formulation of Darcy's problem

The filter cake is modelled by Darcy's equations (6) in domain Ω_c, the solutions of which are both velocity $\underline{v}^c$ and pressure p^c. In the case of the mixed velocity–pressure approach used here, the dual formulation is preferred to express the Darcy's problem, since its solutions $(\underline{v}^c, p^c)$ are defined in the same approximation spaces as the Stokes problem solutions [61]. To describe the weak dual formulation of the problem, we introduce the spaces $Q_c = L^2(\Omega_c)$, $V_c = \{\underline{v}^c \in H(\underline{\nabla}., \Omega_c) | \underline{v}^c \cdot \underline{n} = v_c$ over $\partial\Omega_{c,D}\}$ and $V_c^0 = \{\underline{v}^c \in H(\underline{\nabla}., \Omega_c) | \underline{v}^c \cdot \underline{n} = 0$ over $\partial\Omega_{c,D}\}$, $L^2(\Omega_c)$ and $H(\underline{\nabla}\cdot, \Omega_c)$ corresponding respectively to the Lebesgue space of square integrable functions and Sobolev space.

The weak integral formulation is classically obtained by multiplying the strong form by the velocity and pressure test fields, respectively $\underline{w}^c \in {V_c}^0$ and $q^c \in Q_c$, and then integrating by parts this formulation over the Ω_c domain. Integration by parts of the pressure term in these equations yields the dual formulation of the Darcy's problem and the boundary conditions associated with it. This formulation consists in finding $\left[\underline{v}^c, p^c\right] \in V_c \times Q_c$ such that:

$$< \underline{\nabla} \cdot \underline{v}^c, q^c >_{\Omega_c} = 0 \qquad , \forall q^c \in Q_c \tag{14a}$$

$$< \eta_f \underline{\underline{K}}^{-1} \underline{v}^c, \underline{w}^c >_{\Omega_c} - < p^c, \underline{\nabla} \cdot \underline{w}^c >_{\Omega_c} + < p^c, \underline{w}^c \cdot \underline{n} >_{\partial\Omega_c} = 0 \qquad , \forall \underline{w}^c \in {V_c}^0 \tag{14b}$$

The notation $< \cdot, \cdot >$ designates the L^2 scalar product in Sobolev space.

In equation (14b), the integral on $\partial\Omega_c$ decomposes into $\partial\Omega_{c,D}$, $\partial\Omega_{c,N}$ and Γ. The component on $\partial\Omega_{c,D}$ disappears because the test field is chosen as the variation of the real field and therefore cancels out on this domain boundary. The component on $\partial\Omega_{c,N}$ corresponds to the natural pressure boundary condition. The integral weak dual formulation of Darcy's problem is written as follows [56, 67]:
Find $\left[\underline{v}^c, p^c\right] \in V_c \times Q_c$ such that, $\forall \underline{w}^c \in V_c^0$ and $\forall q^c \in Q_c$:

$$B_c([\underline{v}^c, p^c], [\underline{w}^c, q^c]) = L_c([\underline{w}^c, q^c]) \tag{15}$$

The bilinear form B_c and the linear form L_c are defined by:

$$\begin{aligned} B_c([\underline{v}^c, p^c], [\underline{w}^c, q^c]) =& < \eta_f \underline{\underline{K}}^{-1} \underline{v}^c, \underline{w}^c >_{\Omega_c} - < p^c, \underline{\nabla} \cdot \underline{w}^c >_{\Omega_c} \\ &+ < \underline{\nabla} \cdot \underline{v}^c, q^c >_{\Omega_c} + < p^c, \underline{w}^c \cdot \underline{n} >_{\Gamma} \end{aligned} \tag{16a}$$

$$L_c([\underline{w}^c, q^c]) =< p_{ext,c} \underline{n}, \underline{w}^c >_{\partial\Omega_{c,N}} \tag{16b}$$

3.2. Integral weak formulation of the Stokes' problem

The suspension is modelled by the Stokes' equations (3) in the domain Ω_s, the solutions of which are velocity $\underline{v}^s$ and pressure p^s . The function spaces $Q_s = L^2(\Omega_s)$, $V_s = \left\{\underline{v}^s \in H^1(\Omega_s) | \underline{v}^s = \underline{v} \text{ on } \partial\Omega_s\right\}$ and $V_s^0 = \left\{\underline{v}^s \in H^1(\Omega_s) | \underline{v}^s = 0 \text{ on } \partial\Omega_s\right\}$ are required to introduce the integral weak formulation of the Stokes' problem which is obtained by multiplying the Stokes equations by the test fields $\underline{w}^s \in V_s^0$ and $q_s \in Q_s$ and then integrating this formulation over the domain Ω_s. An integration by parts of these equations reveals the boundary conditions of the problem and reads :
Find $\left[\underline{v}^s, p^s\right] \in V_s \times Q_s$ such that:

$$< \underline{\nabla} \cdot \underline{v}^s, q^s >_{\Omega_s} = 0 \ , \forall q^s \in Q_s \tag{17a}$$

$$\begin{aligned} < 2\eta_s \underline{\underline{\dot{\epsilon}}}(\underline{v}^s), \underline{\underline{\dot{\epsilon}}}(\underline{w}^s) >_{\Omega_s} - < \left(2\eta_s \underline{\underline{\dot{\epsilon}}}(\underline{v}^s) \cdot \underline{n}^s\right), \underline{w}^s >_{\partial\Omega_s} \\ - < p^s, \underline{\nabla} \cdot \underline{w}^s >_{\Omega_s} + < p^s, \underline{w}^s \cdot \underline{n}^s >_{\partial\Omega_s} = 0 \ , \forall \underline{w}^s \in {V_s}^0 \end{aligned} \tag{17b}$$

with $< \underline{A}, \underline{B} >_{\Omega_s} = \int_{\Omega_s} A : B \, d\Omega_s$ the L^2 double dot product. The integral on boundary $\partial\Omega_s$ is decomposed into $\partial\Omega_{s,D}$, $\partial\Omega_{s,N}$ and Γ . The term cancels on $\partial\Omega_{s,D}$ considering the restriction on the velocity in V_s, and the natural boundary condition corresponds to the normal stress prescribed on $\partial\Omega_{s,N}$ (Eq. 3b) : $\underline{\underline{\sigma^s}} \cdot \underline{n^s} = p_{ext,s} \cdot \underline{n^s}$. Using the interface conditions, i.e. the continuity of the normal stress (Eq.7b) and the no-slip condition for the tangential velocity ($\underline{v}^s \cdot \underline{t} = 0$), we obtain the weak formulation of the Stokes equations [56, 67]:
Find $\left[\underline{v}^s, p^s\right] \in V_s \times Q_s$ such that, $\forall \underline{w}^s \in V_s^0$ and $\forall q^s \in Q_s$:

$$B_s([\underline{v}^s, p^s], [\underline{w}^s, q^s]) = L_s([\underline{w}^s, q^s]) \tag{18}$$

The bilinear form B_s and the linear form L_s are defined by:

$$\begin{aligned} B_s([\underline{v}^s, p^s], [\underline{w}^s, q^s]) =& < 2\eta_s \underline{\underline{\dot{\epsilon}}}(\underline{v}^s), \underline{\underline{\dot{\epsilon}}}(\underline{w}^s) >_{\Omega_s} - < p^s, \underline{\nabla} \cdot \underline{w}^s >_{\Omega_s} \\ &+ < \underline{\nabla} \cdot \underline{v}^s, q^s >_{\Omega_s} + < p^c, \underline{w}^s \cdot \underline{n}^s >_{\Gamma} \end{aligned} \tag{19a}$$

$$L_s([\underline{w}^s, q^s]) =< p_{ext,s} \underline{n}^s, \underline{w}^s >_{\partial\Omega_{s,N}} \tag{19b}$$

The same approach must be employed to derive an integral weak formulation with the *Type II* boundary conditions specified in equation (4).

Using a monolithic approach, the weak formulation of the coupled Stokes–Darcy problem is obtained by summing the stabilized variational formulations of either problem [61]. Let us recall

that the same test functions are used to approximate the pressure and velocity fields respectively over the entire domain. The separation of the definition domains for each model is achieved by introducing a Heaviside function H_s, respectively H_c, which is equal to 1, respectively 0, in the Stokes domain and 0, respectively 1, in the Darcy domain. The mixed variational formulation of the Stokes-Darcy coupled problem consists in finding $\underline{v} \in V = V_s \times V_c$ and $p \in Q = Q_s \times Q_c$ such that, $\forall \underline{w} \in V^0 = V_s^0 \times V_c^0$ and $\forall q \in Q$:

$$B([\underline{v}, p], [\underline{w}, q]) = L([\underline{w}, q]) \tag{20}$$

The bilinear form B and the linear form L are defined by:

$$\begin{aligned} B([\underline{v}, p], [\underline{w}, q]) =& < 2\eta_s \underline{\underline{\dot{\epsilon}}}(\underline{v}), \underline{\underline{\dot{\epsilon}}}(\underline{w}) H_s >_\Omega + < \eta_f \underline{\underline{K}}^{-1} \underline{v}, \underline{w} H_c >_\Omega \\ & - < p, \underline{\nabla} \cdot \underline{w} >_\Omega + < \underline{\nabla} \cdot \underline{v}, q >_\Omega \end{aligned} \tag{21a}$$

$$L([\underline{w}, q]) =< p_{ext,s} \underline{n}, \underline{w} >_{\partial\Omega_{s,N}} + < p_{ext,c} \underline{n}, \underline{w} >_{\partial\Omega_{c,N}} \tag{21b}$$

where $\underline{v}|_{\Omega_i} = \underline{v}^i$ and $p|_{\Omega_i} = p^i$, with $i = \{c, s\}$.

3.3. Stabilization of the weak formulations

To solve both the Stokes and Darcy finite element problems, discretization is performed by reducing the variational spaces V and Q (from the respective spaces $(V_s \times Q_s)$ and $(V_c \times Q_c)$) to finite-dimensional spaces V_h and Q_h such that $V_h \subset V$ and $Q_h \subset Q$. The continuous domain Ω is discretized into a domain Ω_h comprising n_e elements, each defining a subdomain Ω_h^e (thus $\Omega_h = \sum_{e=1}^{n_e} \Omega_h^e$).

In this study, in order to keep compatible finite element discretization over the whole domain, both velocity and pressure spaces are approximated using piecewise linear functions (P1/P1 approximations). The V_h and Q_h spaces for the Stokes and Darcy problems are defined using triangles if $dim = 2$, or tetrahedra if $dim = 3$. Due to this approximation, a stabilization method is necessary to solve the problem since the LBB (Ladysenskaya–Brezzi–Babuska) condition is not satisfied [68]. The chosen method is the ASGS (Algebraic SubGrid Scale) method, which allows for the definition of solutions for both the Stokes and Darcy problems in the same approximation spaces. This approach facilitates solving a coupled Stokes–Darcy problem using a monolithic approach [67, 60].

The underlying idea of the ASGS method involves a decomposition of the functional spaces and solutions to approximate the effects, onto the FE discrete solution,of the problem, of the exact solution components that cannot be captured by the mesh. Indeed, the system is decomposed into a coarse-scale system (finite element scale) and a sub-grid system:

- Finite element scale:

$$B([\underline{v_h}, p_h], [\underline{w_h}, q_h]) + \underbrace{B([\underline{v_h}', p_h'], [\underline{w_h}', q_h]')}_{residual} = L([\underline{w_h}, q_h]) \tag{22}$$

- Sub-grid scale:

$$B([\underline{v_h}, p_h], [\underline{w_h}', q_h']) + B([\underline{v_h}', p_h'], [\underline{w_h}', q_h]') = L([\underline{w_h}', q_h']) \tag{23}$$

The stabilized finite element approximation spaces defined in velocity and pressure are now denoted V_h^* and Q_h^* with: $V_h^* \times Q_h^* = (V_h \times Q_h) \bigoplus (V_h^{'} \times Q_h^{'})$. The solution of the sub-grid system (Eq. 23) is expressed as a function of the Finite Element residual of the problem. By replacing the sub-grid terms in the finite element system (Eq. 22) with their new expressions, the stabilized weak formulation is obtained. Additional information about this method for the coupled Stokes–Darcy problem, including the detailed expression of stabilized formulations, can be found in [60, 56, 67, 61].

The stabilized weak formulation is written for the Stokes-Darcy coupled problem as follows:

$$B_{stable}([\underline{v}, p], [\underline{w}, q]) = L_{stable}([\underline{w}, q]) \tag{24}$$

with B_{stable} and L_{stable} defined by:

$$\begin{aligned} B_{stable}([\underline{v}, p], [\underline{w}, q]) = B([\underline{v}_h, p_h], [\underline{w}_h, q_h]) &+ \sum_{e=1}^{n_e} \tau_p < \underline{\nabla} \cdot \underline{v}_h, \underline{\nabla} \cdot \underline{w}_h >_{\Omega_h^e} \\ &+ \sum_{e=1}^{n_e} \tau_u < H_c \eta_f \underline{\underline{K}}^{-1} \underline{v}_h + \underline{\nabla} p_h, -H_c \eta_f \underline{\underline{K}}^{-1} \underline{w}_h + \underline{\nabla} q_h >_{\Omega_h^e} \end{aligned} \tag{25a}$$

$$L_{stable} = L([\underline{w}, q]) \tag{25b}$$

Solving the sub-grid problem involves two stabilization constants τ_u and τ_p defined by [67, 60]:

$$\tau_p = H_c c_p \frac{\eta_f}{K} l_p^2 + H_s c_1 \eta_f \tag{26a}$$

$$\tau_u = H_c \left(c_u \frac{\eta_f}{K} l_u^2 \right)^{-1} h_K^2 + H_s \frac{h_K^2}{c_1 \eta_f} \tag{26b}$$

c_p c_u and c_1 are constants taken equal to 1. l_u and l_p are characteristic lengths defined by $(L_0 h_K)^{1/2}$ where h_K corresponds to the mesh size of the element and L_0 to a characteristic length of the domain.

3.4. Level-Set transport

We have previously noted that a Φ Level-Set function is transported by solving a transport equation (9). By adding to this equation an initial condition and a condition on the incoming boundary, we obtain the following strong form:

$$\frac{\partial \Phi}{\partial t} + \underline{v}_\Gamma . \underline{\nabla} \Phi = 0 \qquad \forall (x, t) \in \Omega \times (0, T) \tag{27a}$$

$$\Phi(x, t = 0) = \Phi_0(x) \qquad \forall x \in \Omega \tag{27b}$$

$$\Phi(x, t) = \Phi(x, t - \Delta t) \qquad \forall x \in \partial\Omega^- \, , \forall t \in (0, T) \tag{27c}$$

with $\Omega = \Omega_c \cup \Omega_s$ and $\partial\Omega = \partial\Omega_c \cup \partial\Omega_s \setminus \Gamma$. $\underline{v}_\Gamma$ is the Level-Set velocity given by mass balance conservation across interface Γ (Eq.(13)). $\partial\Omega^-$ is the incoming edge of $\partial\Omega$, i.e. the section of the boundary through which matter enters.

Problem (27) is solved using a P1 finite element approximation. Finite-dimensional spaces V_h^g and V_h^0 are introduced to approximate spaces $V^g = \{q \in H^1(\Omega) | q = g \text{ on } \partial\Omega^-\}$ and $V^0 = \{q \in H^1(\Omega) | q = 0 \text{ on } \partial\Omega^-\}$. Let $\Phi_h \in V_h^g$ be an approximation of the unknown function Φ. After discretizing the time derivative operator using an implicit Euler scheme, the following weak discrete formulation consists in finding $\Phi \in V_g$ such that:

$$< \frac{\Phi_h(t_n)}{\Delta t}, \Phi_h^* >_{\Omega_h} + \frac{1}{2} < \underline{v}_\Gamma, \underline{\nabla} \left[\Phi_h(t_n) + \Phi_h(t_{n-1})\right] \Phi_h^* >_{\Omega_h} = < \frac{\Phi_h(t_{n-1})}{\Delta t}, \Phi_h^* >_{\Omega_h} \ , \forall \Phi_h^* \in V_h^0 \quad (28)$$

Since the above formulation tends to induce oscillations in the solution for problems dominated by convection, it is stabilized through the classical SUPG (Streamline Upwind/Petrov–Galerkin) method [69]. The principle consists in introducing a test function $\tilde{\Phi}_h^* \in V^0$ of the form :

$$\tilde{\Phi}^* = \Phi^* + \tau_K \underline{v}.\underline{\nabla}\Phi^* \quad (29)$$

with τ_K of the following form: :

$$\tau_K = \frac{1}{2} \frac{h_K}{\|v_{|K}\|} \quad (30)$$

h_K is the mesh size of the element K and $v_{|K}$ is the mean velocity on K. The weak discrete formulation is then written :

$$\begin{aligned} &< \frac{\Phi_h(t_n)}{\Delta t}, \Phi_h^* >_{\Omega_h} + \frac{1}{2} < \underline{v}_\Gamma, \underline{\nabla} \left[\Phi_h(t_n) + \Phi_h(t_{n-1})\right] \Phi_h^* >_{\Omega_h} + \tau_K < \frac{\Phi_h(t_n)}{\Delta t} \underline{v}_\Gamma, \underline{\nabla}\Phi_h^* > \\ &+ \frac{\tau_K}{2} < \underline{v}_\Gamma \cdot \underline{\nabla} \left[\Phi_h(t_n) + \Phi_h(t_{n-1})\right], \underline{v}_\Gamma \cdot \underline{\nabla}\Phi_h^* > = < \frac{\Phi_h(t_{n-1})}{\Delta t}, \Phi_h^* > + \tau_K < \frac{\Phi_h(t_{n-1})}{\Delta t} \underline{v}_\Gamma, \underline{\nabla}\Phi_h^* > \end{aligned} \quad (31)$$

The test function (29) therefore introduces an elliptic term into the weak discrete formulation which creates a numerical diffusion and then a stabilization of the transport equation resolution.

Given the evolution of the convective velocity, the signed distance function property verified by the Level-Set method, i.e. $\|\Delta\phi\| = 1$, may be compromised during the resolution of the transport equation (27). To adress this, a reinitialization step is required to restore this important unit gradient property. In this work, a direct reinitialization method [70, 71, 72] is employed. This method consists in recalculating the Level-Set function from the projection of each node onto the interface, i.e. the shortest distance to the interface. It is more accurate than the method proposed by [73] based on solving a Hamilton–Jacobi type equation. In contrast to the latter, the direct reinitialization method has the advantage of not requiring any tuning of parameters (number of reinitialization steps, reinitialization time step, etc.). While it typically entails a higher computational cost, with an appropriate data structure (e.g., k-d tree), this method can be made efficient.

With the weak formulations in place, the Stokes–Darcy and Level-Set problems are incrementally solved using a weak coupling algorithm (Algorithm.1), relying on the same simplicial mesh.

4. Results and discussions

The validation of a model and its numerical implementation is a crucial step to ensure the reliability and accuracy of the obtained results. In this section, we address the validation of the

Require: ϕ^0 : initial Level-Set function, $\underline{v}^0$: initial velocity, p^0 : initial pressure
Ensure: $\underline{v}$, p, ϕ : updated velocity, pressure, and Level-Set function

$t \leftarrow 0$
while $t < T$ **do**
  Step 1: Solving the fluid problem
  With the interface position defined by $\phi(t)$, solve the Stokes–Darcy coupled system (Eq.(24)) to obtain $\underline{v}(t + \Delta t)$ and $p(t + \Delta t)$
  Step 2: Update the Level-Set function
  Modify the fluid velocity $\underline{v}(t + \Delta t)$ at the interface to account for particle mass conservation (Eq. (13))
  Solve the Level-Set transport equation (Eq.(31)) and update $\phi(t + \Delta t)$
  Step 3: Reinitialize the Level-Set function
  Reinitialize $\phi(t + \Delta t)$ to maintain the signed distance function property
  $t \leftarrow t + \Delta t$
end while
return $\underline{v}(t)$, $p(t)$, $\phi(t)$

Algorithm 1: Weak coupling algorithm.

model presented in the previous sections, focusing on the temporal evolution of the filter cake. This validation is based on various flows relevant to the description of the investigated phenomena. The first two flows studied involve Stokes–Darcy in a rectangular geometry and Stokes–Darcy between two coaxial cylinders. Theses cases enable to assess the model performance under simplified conditions that are representative of many systems. The third case focuses on a three-dimensional (3D) anisotropic flow within an ellipsoid domain. Finally, we will examine a 2D Stokes–Darcy flow in the presence of impermeable and permeable obstacles, representing a first step towards an industrial process model. The simulations presented in this section are carried out on an intel CPU i7-1165G7 laptop in multithreading mode with 4 cores.

4.1. Cake growth in a rectangular domain with Stokes–Darcy flow

We consider here a Stokes–Darcy flow within a 2D rectangular geometry. A filter membrane is placed at the outlet, it has a thickness δ_f and a permeability K_f. This membrane filter, represented as an additional Darcy zone (Figure 4b), induces the accumulation of particles, leading to the formation of a filter cake. The evolving thickness of the cake over time is denoted by $\delta_c(t)$.

Whether under a prescribed inlet volume flow rate or a prescribed inlet pressure, [16] have analytically determined the thickness $\delta_c(t)$ for this configuration, it writes:

- Prescribed inlet pressure:

$$\delta_c(t) = R_f K_c \left[\left(\frac{\left(R_f + \delta_c(0)/K_c\right)^2}{R_f^2} + 2t \frac{\phi_s}{(\phi_c - \phi_s)} \frac{\Delta p}{\eta_f} \frac{1}{R_f^2 K_c} \right)^{1/2} - 1 \right] \tag{32}$$

Dimensions ($L \times h =$)	Physical parameters	Numerical parameters
$5\ 10^{-2}$ m $\times\ 10^{-2}$ m	$\Delta p = 10^5$ Pa, $\eta_f = 10^{-3}$ Pa.s	Mesh:
	$K_c = 10^{-13}$ m^2, $K_f = 10^{-15}$ m^2	$nb^{nodes} = 2734$
	$\delta_c(0) = 0$ m, $\delta_f = 10^{-3}$ m	$nb^{DOF} = 8202$
	$\phi_c = \phi_m = 0.6$, $\phi_s = 0.1$	Fixed time step:
		$\Delta t = 0.1$ s

Table 1: Simulation parameters for the *1D-flow* rectangular geometry. nb^{nodes} and nb^{DOF} respectively denote the number of nodes and the number of degrees of freedom.

- Prescribed inlet flow rate (velocity v known and constant):

$$\delta_c(t) = \delta_c(0) + \frac{\phi_s}{(\phi_c - \phi_s)} v\ t \tag{33}$$

where Δp is the imposed pressure drop, $\delta_c(0)$ is the initial cake thickness, ϕ_s (resp. ϕ_c) is the particle concentration of the suspension (resp. the cake), K_c (resp. K_f) is the permeability of the cake (resp. filter) and $R_c = \delta_c(t)/K_c$ (resp. $R_f = \delta_f/K_f$) is the hydraulic resistance of the cake (resp. filter).

In this part, we numerically solve this problem and subsequently compare the obtained results against the aforementioned analytical solutions. First, the fluid flows under prescribed inlet pressure condition. The simulation parameters are detailed in Table 1 and Figure 4a and will be referred to as *1D-flow* since homogeneous *Type II* conditions (impervious walls) are considered along the lateral edges ($y = 0$ and $y = h$).

In Figure 5 is plotted the numerical cake thickness $\delta_c(t)$ in comparison with the analytical solution given by Eq.(32). Concurrently, Figure 6 illustrates the absolute ($\left|\delta_c^{numerical} - \delta_c^{analytical}\right|$) and relative ($\left|\frac{\delta_c^{numerical} - \delta_c^{analytical}}{\delta_c^{analytical}}\right|$) errors between the two solutions. Our observation reveals a remarkable concordance between the results, characterized by a low overall error. Notably, the relative error (Figure 6a) exhibits high values in the initial increments, attributable to the very small values of $\delta_c^{analytical}$ at the beginning of the computation. This observation is corroborated by the corresponding solution and absolute error (Figures 5-6b), the latter showing a maximal absolute lower than $1E-4\ m$ for dimensions in the range of $1E-2\ m$.

Furthermore, Figure 4 presents the state of the problem at different times, highlighting the evolution of the zero iso-value of the Level-Set function. Consistent with the prescribed boundary and initial conditions, the filter cake remains invariant along the y-axis. Sub-figures 4c and 4d also depict the velocity and pressure fields, respectively. We can verify that the problem reveals itself to be essentially one-dimensional, with velocity and pressure confined in the x-direction.

Figure7a illustrates the robust conservation of volume. Indeed, it can be seen that the volume flow rate at the inlet remains consistent with that at the outlet throughout the filling process. Furthermore, Figure7b depicts the proper conservation of particle mass ensuring that the numerical

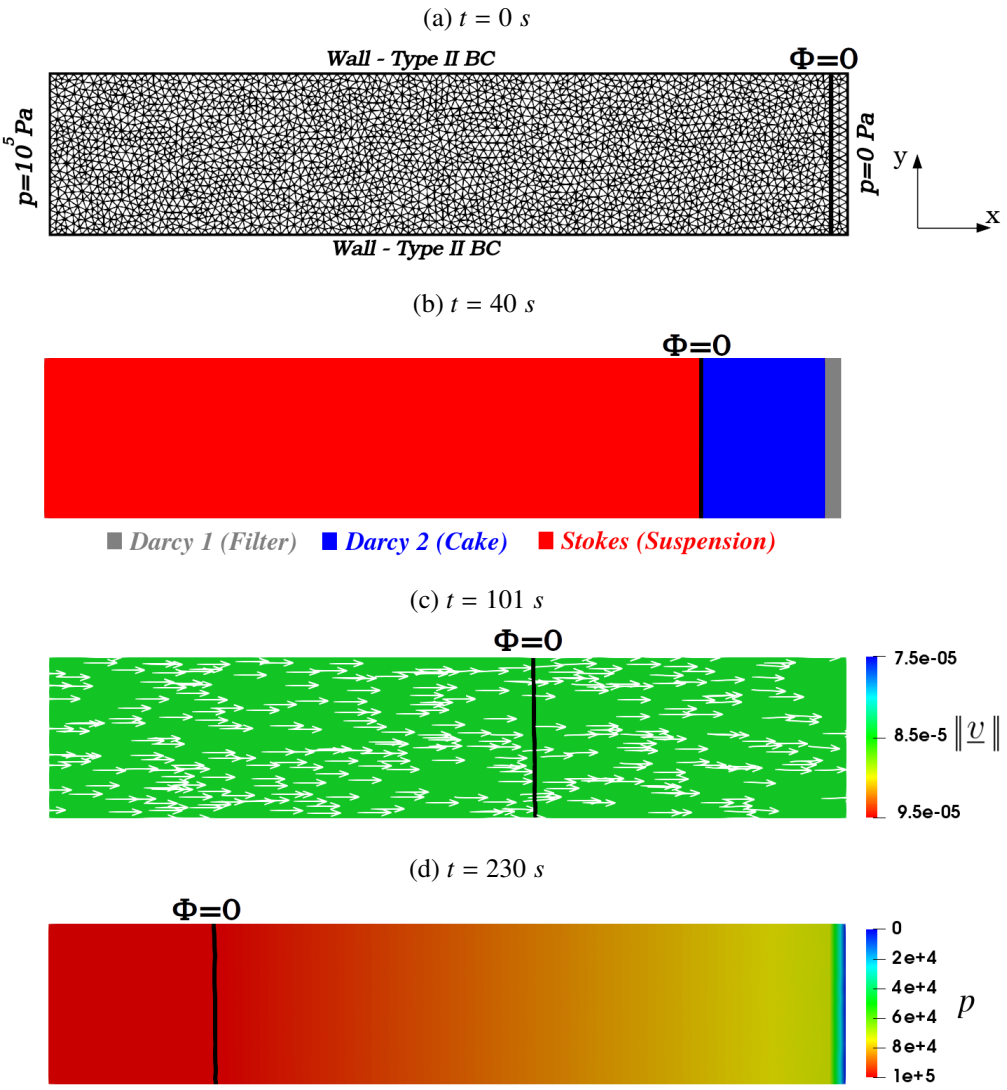

Figure 4: Prescribed inlet pressure condition for *1D-flow*: temporal progression of the zero iso-value of the Level-Set function (black line). Additionally depicted are: (a) the mesh and boundary conditions, (b) delineation of physical zones, (c) representation of velocity field and magnitude, and (d) visualization of pressure field.

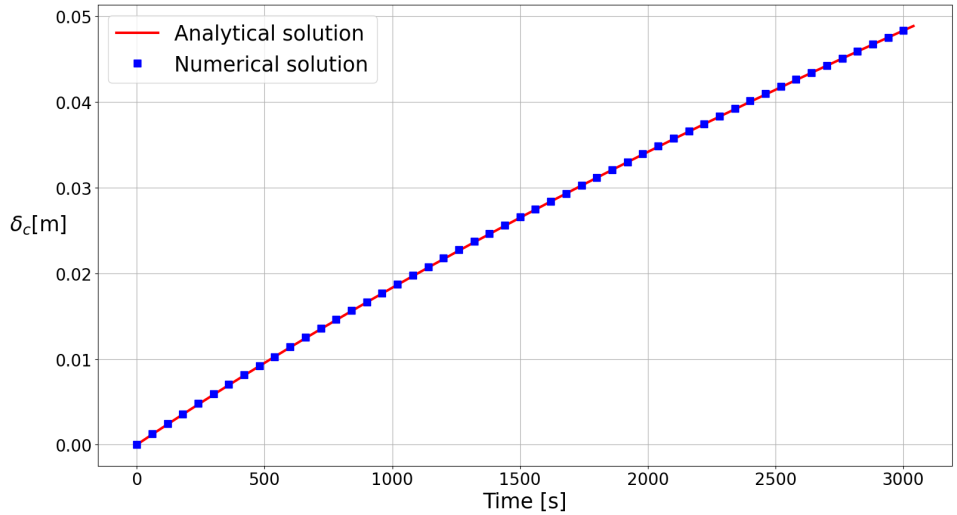

Figure 5: Prescribed inlet pressure condition for : computed filter cake thickness *vs* time, compared with the analytical solution of Eq.(32).

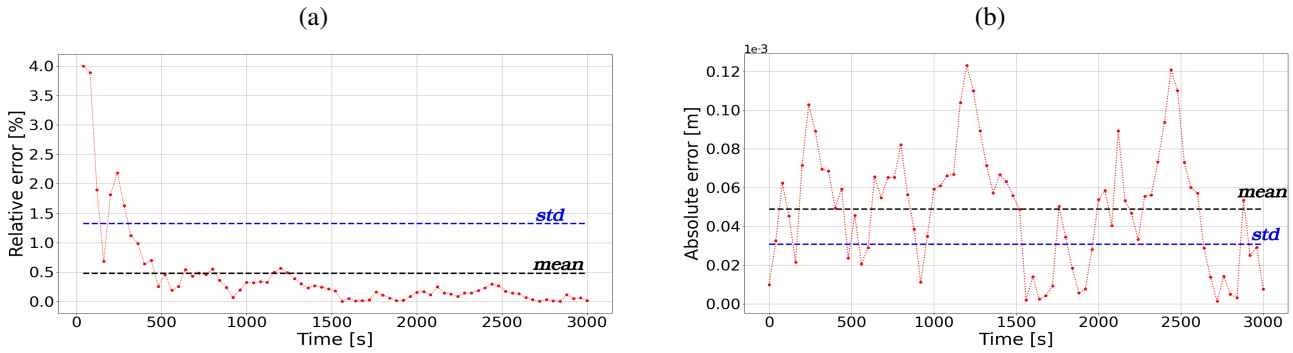

Figure 6: Prescribed inlet pressure condition: analysis of discrepancy between the cake thickness computed $\delta_c(t)$ and calculated from Eq.(32), presented through (a) relative error $\left|\frac{\delta_c^{numerical}-\delta_c^{analytical}}{\delta_c^{analytical}}\right|$ and (b) absolute error $\left|\delta_c^{numerical}-\delta_c^{analytical}\right|$.

	$nb^{nodes} = 716$	$nb^{nodes} = 2\,734$	$nb^{nodes} = 10\,815$
Mean relative error	0.80%	0.48%	0.33%
Total mass variation	0.63%	0.038%	0.028%

Table 2: Mean relative error and total mass variation for different mesh density.

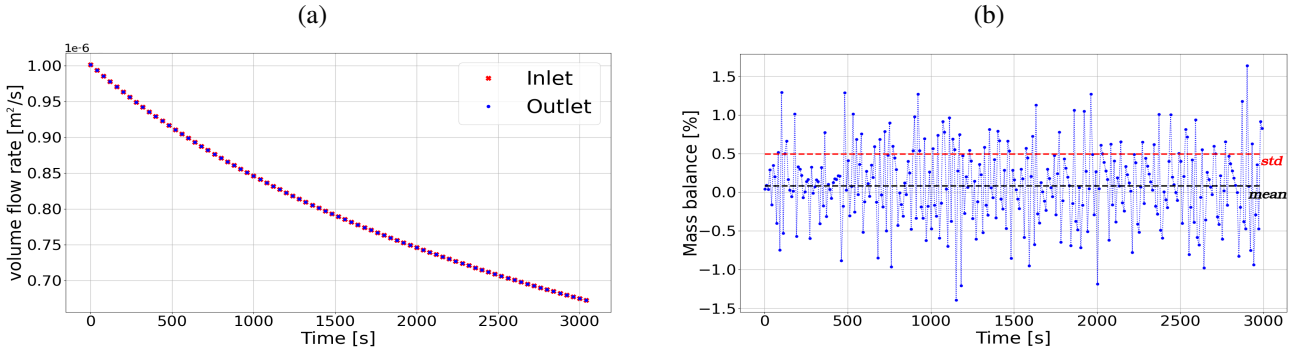

Figure 7: Prescribed inlet pressure condition: (a) comparison of volume flow rates at the inlet and outlet over time, (b) evolution of mass balance ($\frac{J\phi_s dt+\phi_s d\delta_c-\phi_c d\delta_c}{J\phi_s dt}$) with respect to time.

solution adheres to the mass balance equation [16] : $J\phi_s dt+\phi_s d\delta_c = \phi_c d\delta_c$. Here, $J\phi_s dt$ represents the quantity of particles per unit time supplied by the incoming flow, $\phi_s d\delta_c$ denotes the quantity of particles per unit time lost by the suspension, and $\phi_c d\delta_c$ denotes the quantity of particles per unit time deposited in the cake. In Figure 7b, the variable $\frac{J\phi_s dt+\phi_s d\delta_c-\phi_c d\delta_c}{J\phi_s dt}$ is plotted as a function of time, it demonstrates clearly that the loss and gain of particle mass exhibit qualitative equivalence. Additionally, the cumulative sum over time (curve integration) of these mass variations yields a total mass variation of +0.038%. Consequently, particle mass is effectively conserved during the filling process. Additionally, this case study was conducted with two other mesh sizes, $nb^{nodes} = 716$ and $nb^{nodes} = 10815$, and the results for the mean relative error and the total mass variation are presented in Table 2. It is evident that as the mesh size decreases, both the error and the mass loss are reduced. Furthermore, even with a coarser mesh ($nb^{nodes} = 716$), the error and mass total variation remain within acceptable limits. This demonstrates one of the advantages of the Level-Set method, which does not require any extensive remeshing and mesh adaptation, unlike other methods.

Instead of applying pressure at the inlet, a constant velocity $\underline{v} = (2.10^{-3}, 0, 0)$ m/s is now imposed, ensuring a consistent volume flow rate over time. Given the constancy of velocity in this scenario, the analytical time profile of pressure can be readily deduced from Darcy's equations. The findings presented herein are highly compelling. A meticulous comparison of the computed cake thickness and pressure with their analytical counterparts reveals an outstanding agreement (refer to Figs. 8,9,10). Moreover, the preservation of particle mass, as depicted in Figure11, is notable, with a mere +0.064% total mass variation observed during the whole cake growth process.

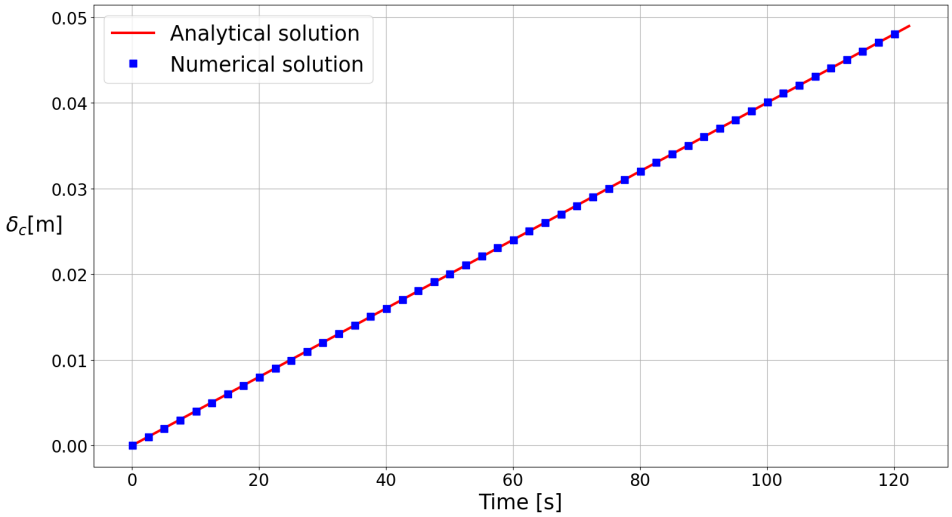

Figure 8: Prescribed inlet flux condition: computed filter cake thickness *vs* time, compared with the analytical solution of Eq.(33).

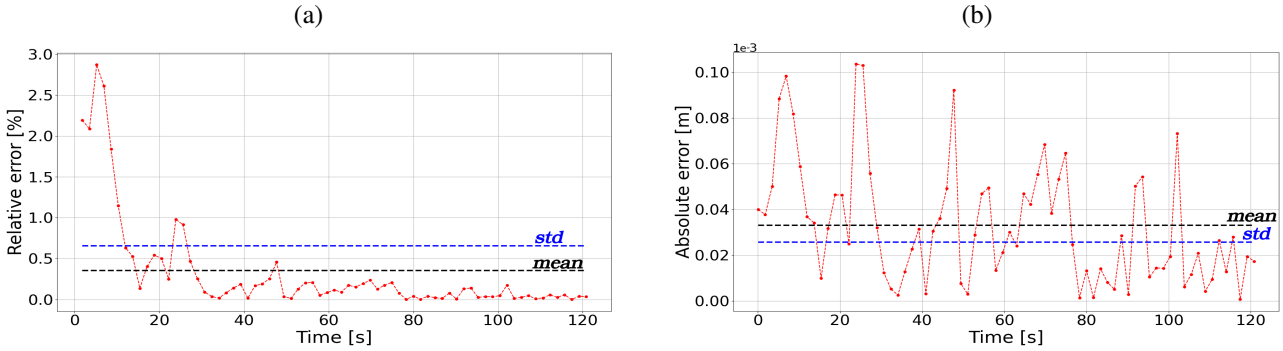

Figure 9: ¨rescibed inlet flux condition: analysis of discrepancy between the computed thickness $\delta_c(t)$ and the analytical thickness described by Eq.(33), presented through (a) relative error $\left|\frac{\delta_c^{numerical}-\delta_c^{analytical}}{\delta_c^{analytical}}\right|$ and (b) absolute error $\left|\delta_c^{numerical}-\delta_c^{analytical}\right|$.

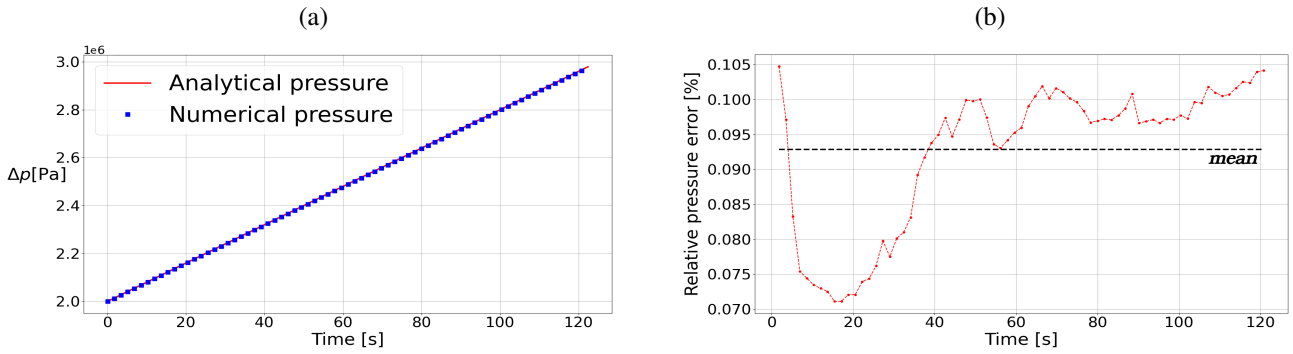

Figure 10: Prescribed inlet flux condition: (a) analytical and numerical pressure plotted against time. (b) Relative error between analytical and numerical pressure.

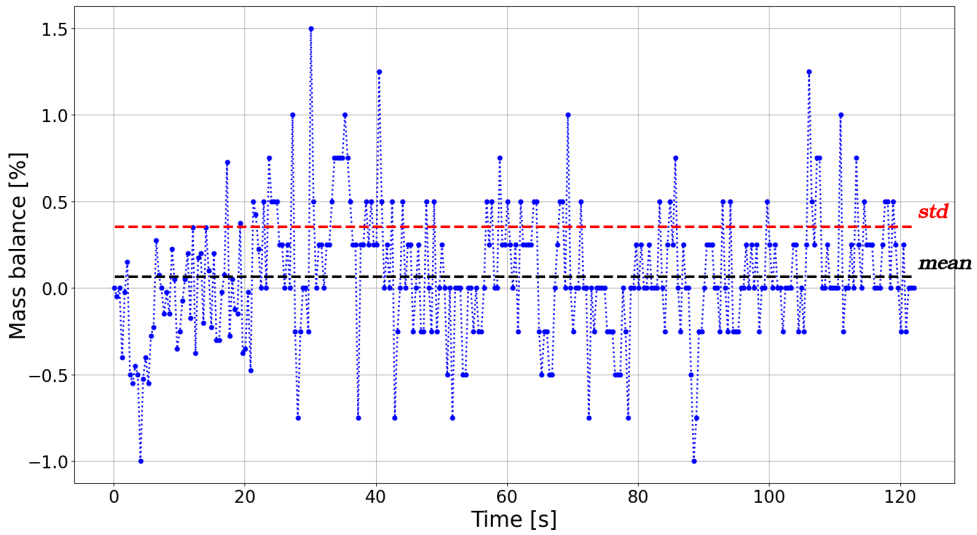

Figure 11: Prescribed inlet flux condition: evolution of mass balance ($\frac{J\phi_s dt+\phi_s d\delta_c-\phi_c d\delta_c}{J\phi_s dt}$) with respect to time.

The outcomes presented in this section are notably satisfactory, reflecting the effectiveness of the proposed numerical model. The computation time for these cases is reasonable, approximately 57 minutes for the prescribed inlet pressure case and 11 minutes for the prescribed inlet flux case. A good agreement is observed when comparing the numerical solutions with the analytical ones provided by [16]. Additionally, the preservation of particle mass during the filling process is consistently well-maintained. Moreover, [17] conducted experimental dead-end filtration assessments employing suspensions of varying concentrations, with measurements of filter cake thickness over time. The successful alignment of the results obtained from the present model with these experimental measurements, as illustrated in Figure 12, further underscores the model reliability in representing this type of problem.

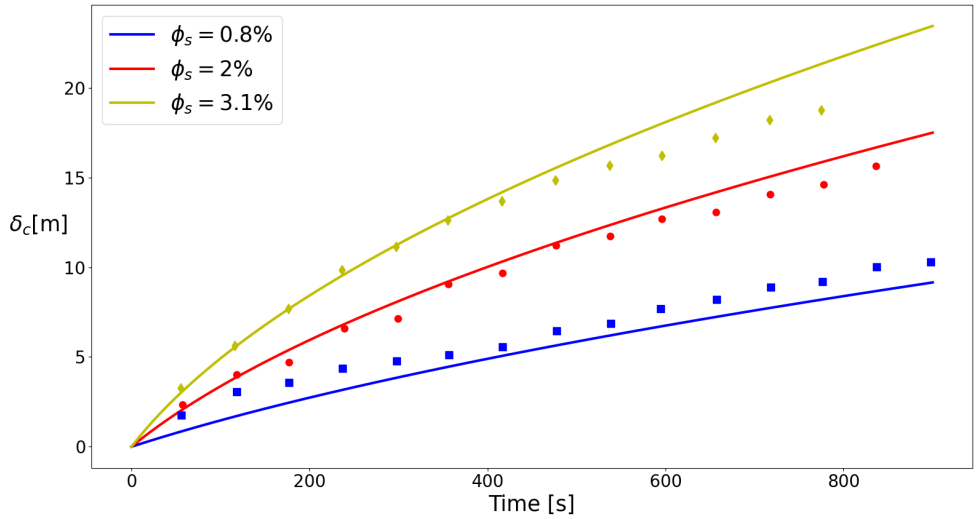

Figure 12: Temporal evolution of filter cake thickness for various initial concentrations, juxtaposed with experimental measurements from [17], represented by markers. The cake porosity chosen here is 0.35 ($\phi_c = 0.65$) [74].

4.2. Cake growth in a Stokes–Darcy flow between two coaxial cylinders

We now examine a more intricate flow scenario, specifically a 2D purely radial flow, illustrated in Figure13a. The geometry under investigation comprises two coaxial cylinders with inner radius $R_i = 5 \times 10^{-3}$ m and outer radius $R_o = 2 \times 10^{-2}$ m. Introducing a filter membrane on the outer cylinder leads to the formation of a filter cake between the two cylinders. This filter is positioned at a radius $R_m = 1.95 \times 10^{-2}$ m and a pressure of 10^5 Pa is prescribed on the surface of the inner cylinder (see Figure13a-13b). The relevant problem parameters are outlined in Figure13a and Table3. Given the purely radial nature of the flow, an analytical solution can be readily derived. [16] provides the following analytical equation for this radial flow:

$$\frac{d\delta_c}{dt} = \frac{\phi_s \Delta p}{(\phi_c - \phi_s)\eta_f} \frac{R_m}{\left(R_f + \frac{R_m}{K_c} \ln\left(\frac{R_m}{R_m - \delta_c}\right)\right)(R_m - \delta_c)} \tag{34}$$

Dimensions	Physical parameters	Numerical parameters
$R_i = 5 \times 10^{-3}$ m	$\Delta p = 10^5$ Pa, $\eta_f = 10^{-3}$ Pa.s	Mesh:
$R_m = 1.95 \times 10^{-2}$ m	$K_c = 10^{-13}$ m^2, $K_f = 10^{-15}$ m^2	$nb^{nodes} = 17982$
$R_0 = 2 \times 10^{-2}$ m	$\delta_c(0) = 0$ m, $\delta_f = 5.10^{-4}$ m	$nb^{DOF} = 53946$
	$\phi_c = \phi_m = 0.6$, $\phi_s = 0.1$	Fixed time step:
		$\Delta t = 0.03$ s

Table 3: Simulation parameters for the coaxial cylinder case.

Let us clarify that R_f refers to the hydraulic resistance of the filter, while R_m designates the radius at which it is positioned. In [16], the filter is not considered as a part of the flow area, in contrast to our approach. This is why in our case, in the numerator of Eq.(34), R_m must be replaced by R_o.

In the present case study, as in the previous one, our objective is to juxtapose the results of our simulation with the analytical solution derived by [16] (Eq.(34)). For this purpose, Figure 14 illustrates a new plot of the computed cake thickness $\delta_c(t)$ (measured along the x-axis), compared with the solution provided by Eq.(34). Simultaneously, we plot the relative and absolute errors between both solutions in Figure 15. The findings indicate a high degree of consistency, characterized by an low overall mean error (2.42×10^{-5} m for mean absolute error).

In Figure 13 is plotted the change in the zero iso-value of the Level-Set function. A quasi-1D problem seems to emerge, specifically expressed in the radial direction, with cake shape remaining invariant in the orthoradial direction. This is corroborated by the velocity and pressure distributions presented in Figs.13c-13d. The simulation of the entire geometry, instead of an axisymmetric resolution, is justified by examining the model capacity to accurately represent the displacement of the Level-Set in this type of configuration. The transport of a circular Level-Set can indeed be non-trivial. To this end, Figure 16 illustrates the time-dependent average radius of curvature of the Level-Set iso-zero. More precisely, at each time is computed the mean distance from each point on the Level-set zero iso-value to the center of the cylinders. In this figure, the numerical curvature radius is compared to the analytical counterpart (Eq.(34)), demonstrating a highly satisfactory concordance between the two.

This case study is concluded with an analysisn of the volume and particle mass conservation. Figure 17a reveals the effective volume conservation, and notably that the volume flow rate at the inlet consistently matches the one at the outlet over the entire duration of the filling process. Additionally, the conservation of particle mass can be analyzed from Figure 17b, it confirms that the numerical solution nicely fits to the mass balance equation from [16]: $JR_o\phi_s dt + \phi_s(R_m - \delta_c)d\delta_c = \phi_c(R_m - \delta_c)d\delta_c$, with $JR_o\phi_s dt$ the quantity of particles per unit time supplied by the incoming flow, $\phi_s(R_m - \delta_c)d\delta_c$ the quantity of particles per unit time lost by the suspension and $\phi_c(R_m - \delta_c)d\delta_c$ the quantity of particles per unit time deposited in the cake. Figure 17b represents the temporal change of the quantity $\frac{JR_o\phi_s dt + \phi_s(R_m-\delta_c)d\delta_c - \phi_c(R_m-\delta_c)d\delta_c}{JR_o\phi_s dt}$ that yields a cumulative sum over time (curve integration) of the mass variations of -0.244%. Consequently, the conservation of particle mass is well-maintained during the filling process.

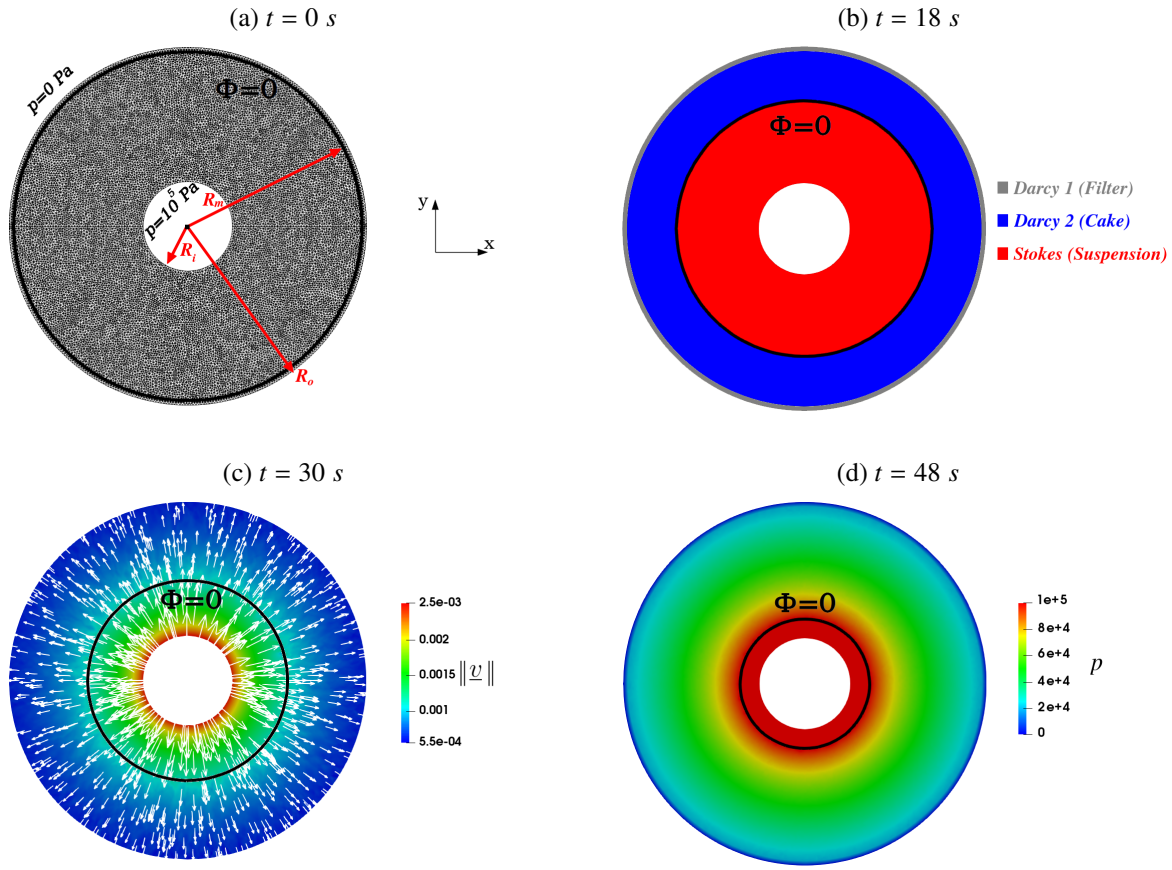

Figure 13: Coaxial cylinder case: temporal progression of the zero iso-value of the Level-Set function (black line). Additionally depicted are: (a) the mesh and boundary conditions, (b) delineation of physical zones, (c) representation of velocity field and magnitude, and (d) visualization of pressure field.

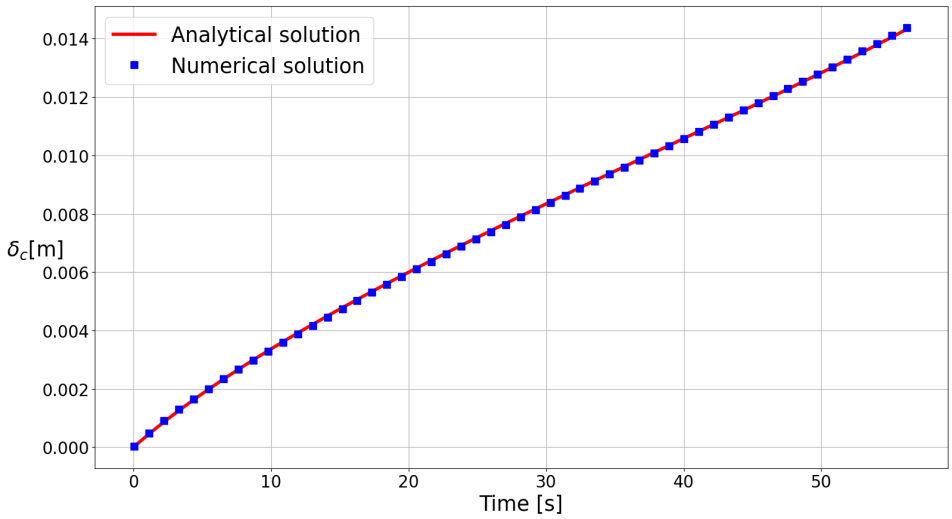

Figure 14: Coaxial cylinder case: computed filter cake thickness *vs* time compared with the analytical solution of Eq.(34).

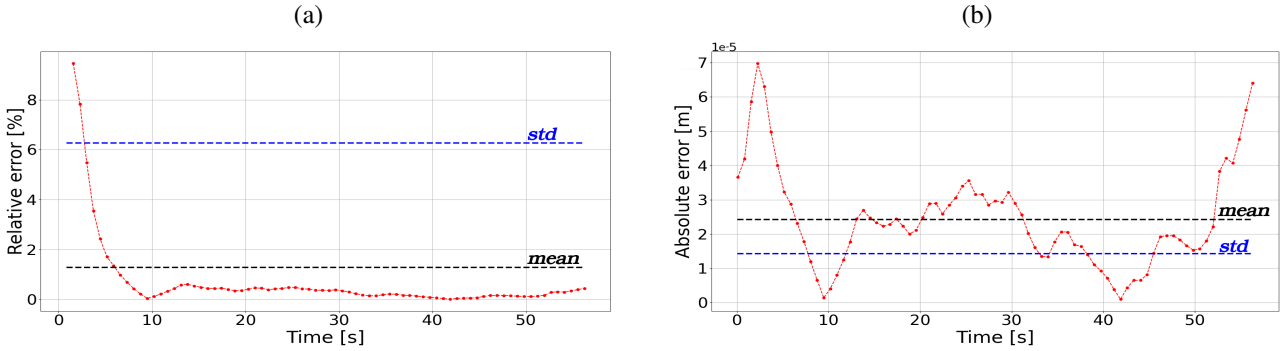

Figure 15: Coaxial cylinder case: analysis of discrepancy between the computed thickness $\delta_c(t)$ and the analytical thickness described by Eq.(34), presented through (a) relative error $\left|\frac{\delta_c^{numerical}-\delta_c^{analytical}}{\delta_c^{analytical}}\right|$ and (b) absolute error $\left|\delta_c^{numerical}-\delta_c^{analytical}\right|$.

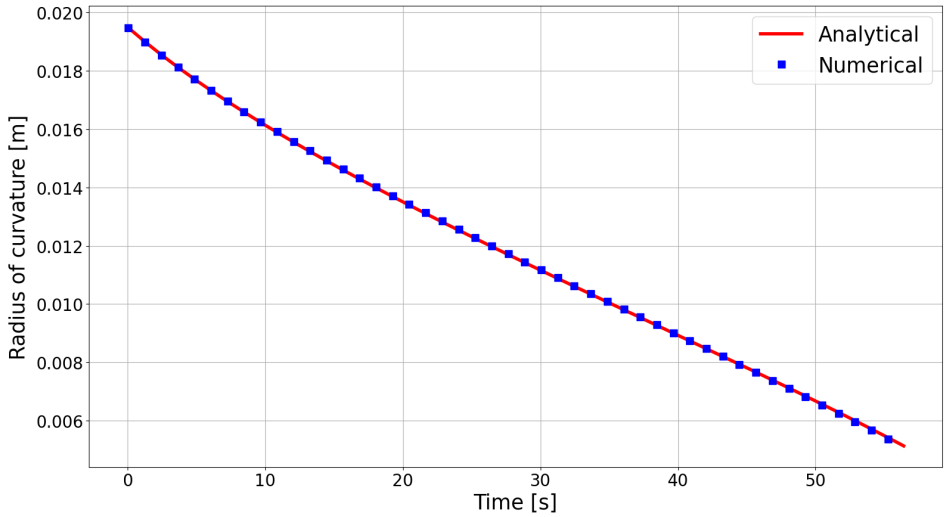

Figure 16: Coaxial cylinders case: computed time-dependent average radius of curvature of the Level-set zero iso-value compared with its analytical counterpart.

(a) (b)

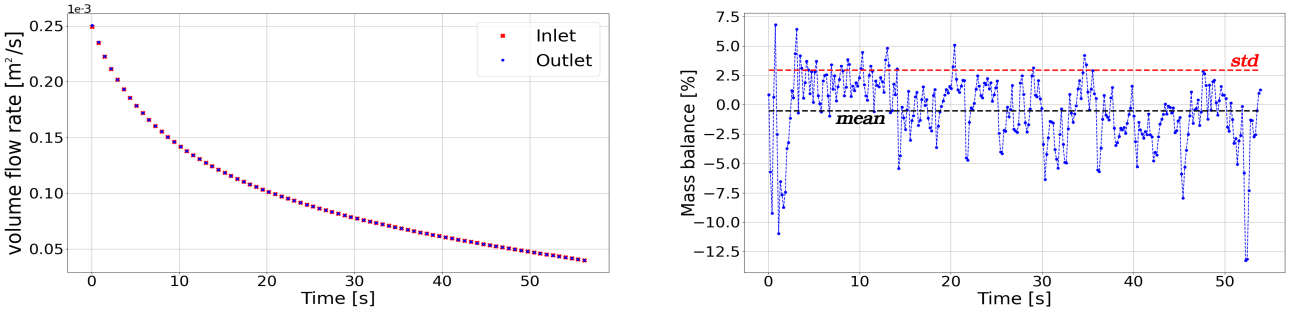

Figure 17: Coaxial cylinder case: (a) comparison of volume flow rates at the inlet and outlet over time, (b) change in mass balance ($\frac{JR_o\phi_s dt+\phi_s(R_m-\delta_c)d\delta_c-\phi_c(R_m-\delta_c)d\delta_c}{JR_o\phi_s dt}$) with respect to time.

Dimensions	Physical parameters	Numerical parameters
$r_z^o = 5.00 \times 10^{-3}$ m	$\Delta p = 10^5$ Pa, $\eta_f = 10^{-3}$ Pa.s	Mesh:
$r_z^i = 1.25 \times 10^{-3}$ m	$k_x = 9.10^{-14}$ m^2, $k_y = 10^{-14}$ m^2	$nb^{nodes} = 91\ 120$
$r_z^f = 1.55 \times 10^{-3}$ m	$k_z = 4.10^{-14}$ m^2, $\underline{\underline{K}}_f = \underline{\underline{K}}_c$	$nb^{DOF} = 364\ 480$
$\frac{r_y^o}{r_z^o} = \frac{r_y^i}{r_z^i} = \frac{r_y^f}{r_z^f} = 0.5$	$\phi_c = \phi_m = 0.6$, $\phi_s = 0.1$	Variable time step
$\frac{r_x^o}{r_z^o} = \frac{r_x^i}{r_z^i} = \frac{r_x^f}{r_z^f} = 1.5$		

Table 4: Simulation parameters for the ellipsoids case.

In summary, the obtained results are deemed satisfactory, characterized by an overall low error and achieved within a reasonable computation time of approximately 4 hours with a fixed time step. The careful analysis confirms the correct conservation of both volume and particle mass throughout the studied process.

4.3. 3D anisotropic cake growth in a Stokes–Darcy flow between two ellipsoids

This section presents a study of a 3D orthotropic radial flow between two ellipsoids. In contrast to the previous cases, this scenario is more complex as the evolution of the filter cake differs in all three directions. The outer ellipsoid has semi-axes of length $r_x^o = 7.5 \times 10^{-3}$ m, $r_y^o = 2.5 \times 10^{-3}$ m, $r_z^o = 5 \times 10^{-3}$ m, while those of the inner cylinder are $r_x^i = 1.875 \times 10^{-3}$ m, $r_y^i = 6.25 \times 10^{-4}$ *m*, $r_z^i = 1.25 \times 10^{-3}$ m. An ellipsoidal filter membrane is positioned near the inner ellipsoid with semi-axes $r_x^f = 2.325 \times 10^{-3}$ m, $r_y^f = 7.75 \times 10^{-4}$ m and $r_z^f = 1.55 \times 10^{-3}$ m. A pressure of 10^5 Pa is applied to the outer ellipsoid, leading to the accumulation of particles from the inner ellipsoid to the outer one (Figure20).

For better validation, the permeability cake is assumed to be anisotropic, and described by the following orthotropic tensor:

$$\underline{\underline{K}}_c = \begin{pmatrix} k_x & 0 & 0 \\ 0 & k_y & 0 \\ 0 & 0 & k_z \end{pmatrix}_{(\underline{x},\underline{y},\underline{z},)} \tag{35}$$

The permeability of the filter is set equal to that of the cake $\underline{\underline{K}}_f = \underline{\underline{K}}_c$, for an easier calculation of the analytical solution. Indeed, under certain conditions, it is possible to derive an analytical solution for this problem. In the case of a purely radial isotropic 3D flow between two spheres with respective radii r_i and r_o, the combination of Darcy's equation (5b) with the mass conservation equation (5a) yields the basic 1D ODE:

$$\frac{1}{r^2}\frac{d}{dr}\left(r^2\frac{dp}{dr}\right) = 0. \tag{36}$$

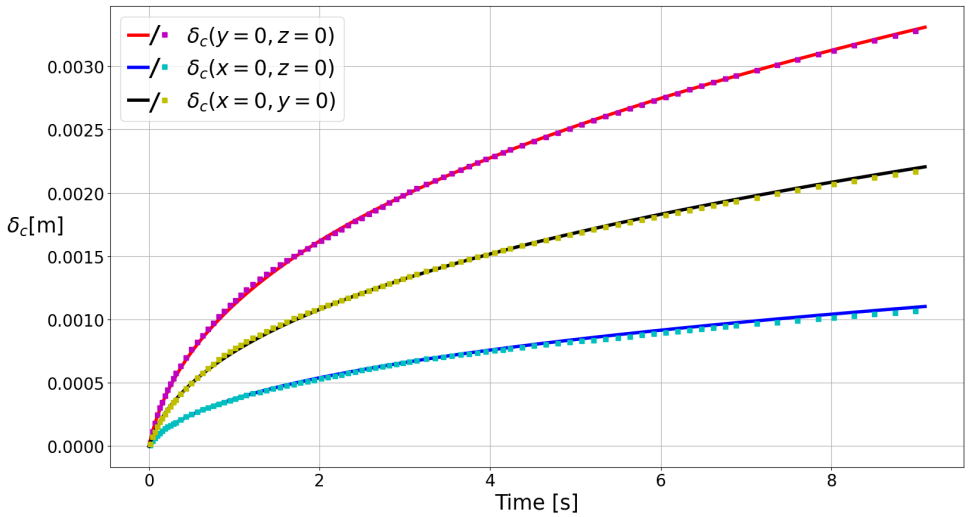

Figure 18: Ellipsoids case: computed filter cake thickness *vs* time (dotted line), compared with the analytical solution of Eqs.(39) (solid line).

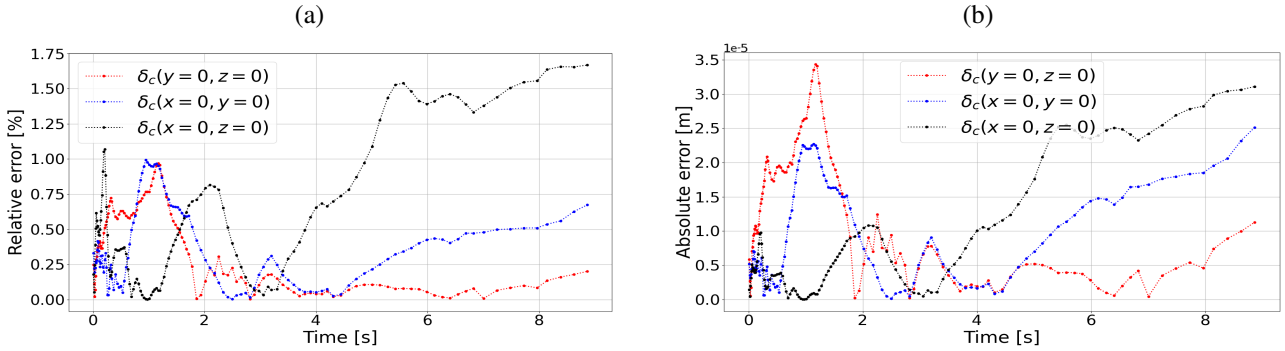

Figure 19: Ellipsoids case: analysis of discrepancy between the computed cake thickness $\delta_c(t)$ and the analytical thickness described by Eqs.(39), presented through (a) relative error $\left|\frac{\delta_c^{numerical}-\delta_c^{analytical}}{\delta_c^{analytical}}\right|$ and (b) absolute error $\left|\delta_c^{numerical}-\delta_c^{analytical}\right|$.

With the above equation, the analytical temporal evolution of cake thickness can be easily derived:

$$\frac{d\delta_c}{dt} = \frac{\phi_s}{(\phi_c - \phi_s)} \frac{\Delta p}{\eta_f} K_c \frac{r^i}{(r - r^i)r} \tag{37}$$

In the orthotropic case under consideration, the principle for solving analytically involves transforming the orthotropic system into an isotropic system of permeability K_c through a change of variables, making it simpler to solve [75, 76]. The transformation to the isotropic coordinate system (X, Y, Z) is accomplished using the following relations [75]:

$$X = \left(\frac{K_c}{k_x}\right)^{1/2} x, \qquad Y = \left(\frac{K_c}{k_y}\right)^{1/2} y, \qquad Z = \left(\frac{K_c}{k_z}\right)^{1/2} z \tag{38}$$

with $K_c = \left(k_x k_y k_z\right)^{1/3}$. The problem then becomes analogous to that of Eq.(36). The inverse transformation allows deducing, for the anisotropic problem, the temporal variation of the cake thickness along the three axes x, y, and z:

$$\frac{d\delta_c(x, y = 0, z = 0)}{dt} = \frac{\phi_s}{(\phi_c - \phi_s)} \frac{\Delta p}{\eta_f} k_x \frac{r_x^i}{(x - r_x^i)x} \tag{39a}$$

$$\frac{d\delta_c(y, x = 0, z = 0)}{dt} = \frac{\phi_s}{(\phi_c - \phi_s)} \frac{\Delta p}{\eta_f} k_y \frac{r_y^i}{(y - r_y^i)y} \tag{39b}$$

$$\frac{d\delta_c(z, x = 0, y = 0)}{dt} = \frac{\phi_s}{(\phi_c - \phi_s)} \frac{\Delta p}{\eta_f} k_z \frac{r_z^i}{(z - r_z^i)z} \tag{39c}$$

These three equations are independent of each other. It should be noted that this analytical solution is only feasible if the ratios of the semi-major axes of all ellipsoids satisfy:

$$\frac{r_x}{r_y} = \sqrt{\frac{k_x}{k_y}}, \qquad \frac{r_x}{r_z} = \sqrt{\frac{k_x}{k_z}}, \qquad \frac{r_y}{r_z} = \sqrt{\frac{k_y}{k_z}} \tag{40}$$

Once again, our aim is to compare the results of our numerical simulation with the solutions provided by Eqs.39. The problem parameters are presented in Figure20a and Table 4. Based on the symmetry of the problem, the simulation is conducted on one-eighth of the geometry. In Figure18 are plotted the computed cake thickness along the three axes, compared with those derived from Eqs.39. The results exhibit excellent agreement, as evidenced by the low errors displayed in Figure19 (relative errors lower than 1.75%). These errors can be further minimized with a finer mesh size, especially in the *y*-direction. Figure 20 illustrates the system state at various moments, revealing an ellipsoidal cake, as anticipated by Eqs.39-40. The nature of the problem is distinctly three-dimensional, as evidenced by the velocity and pressure distributions (Figs.20c-20d). The displacement of the Level-Set is effectively managed by the numerical resolution. The computation time is approximately 34 hours on a laptop but can be largely reduced in HPC. Thus, the current numerical model accurately describes this type of anisotropic 3D cake formation. It is noteworthy to emphasize the importance of employing a Level-Set reinitialization method for high-quality results.

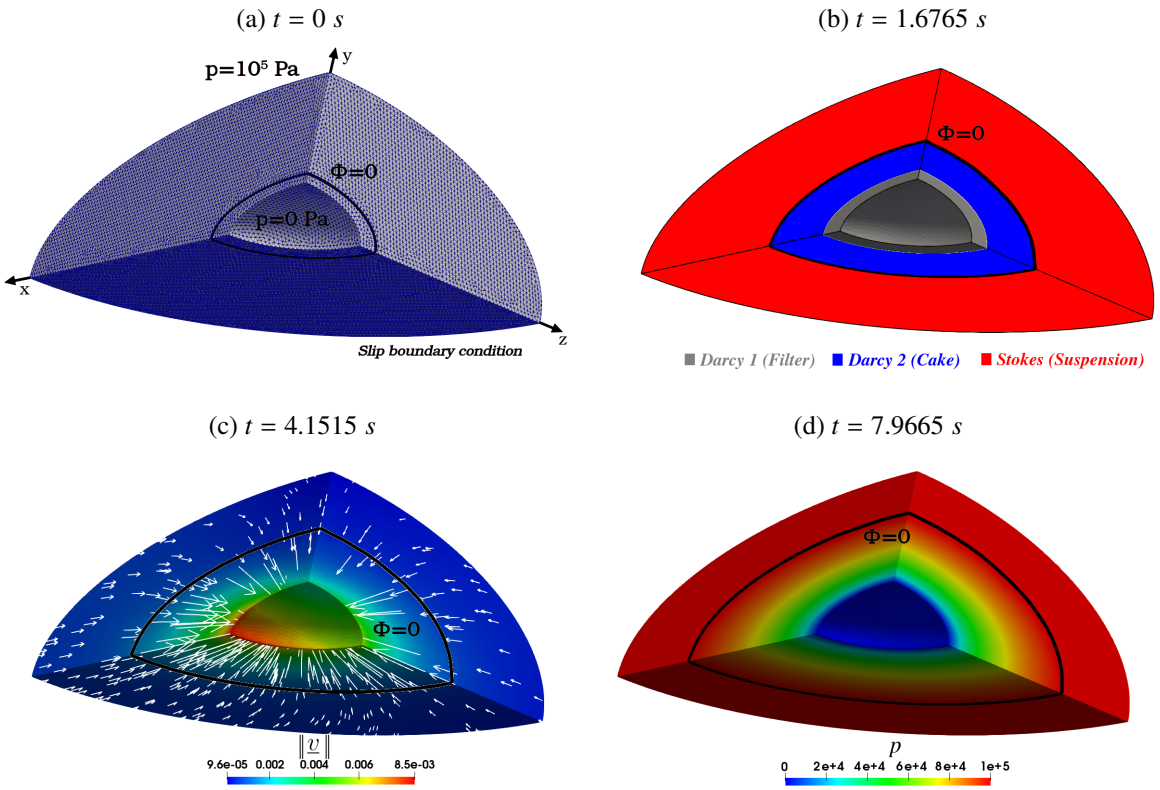

Figure 20: Ellipsoids case: temporal progression of the Level-Set iso-zero (black line). Additionally depicted are: (a) the mesh and boundary conditions, (b) delineation of physical zones, (c) representation of velocity, and (d) visualization of pressure.

As a conclusion of these test-cases, it must be pointed out that coupling Stokes–Darcy regions with permeabilities of 10^{-13} – 10^{-15} m^2 and moving boundaries is not trivial. This can be achieved only with specific minimal ingredients [56, 61, 62] .

4.4. Cake growth in a Stokes–Darcy flow with tows

In this section, we present a numerical simulation of a 2D case study representative of the slurry cast process commonly used in manufacturing composite materials. This process involves the injection of particles into fibrous structures. As illustrated in Figure 1, the filling may not be optimal, leaving areas without particles, known as macropores. These macropores can have a significant influence on the final properties of the composite material. As with previous validations, this case study is modelled using a coupling between the Stokes' equations, describing the motion of the suspension, and the Darcy's equations, characteristic of the filter cake. Firstly, tows containing hundreds of individual fibers are modelled as obstacles in the domain, impermeable to fluid and particles. The simulation geometry is illustrated in Figure 21a, where the 2D domain represents a very small cross-section (only two tows of fibers are considered) of the slurry cast process. The tows are positioned regularly in the domain. In the actual process, their arrangement is typically more complex, and their volume fraction is larger. The simulation parameters are sum-

Dimensions	Physical parameters	Numerical parameters
Geometry:	$\Delta p = 10^5$ Pa, $\eta_f = 10^{-3}$ Pa.s	Mesh (impermeable case):
1.3 mm × 1.5 mm	$K_c = 10^{-13}$ m^2, $K_f = 10^{-15}$ m^2	nb^{nodes} = 7 913
Tows (ellipses):	$\delta_c(0) = 0$ m, $\delta_f = 6.10^{-4}$ m	nb^{DOF} = 23 739
$r_x = 0.4$ mm	$\phi_c = \phi_m = 0.6$, $\phi_s = 0.15$	Mesh (permeable case):
$r_y = 0.2$ mm		nb^{nodes} = 11 804
		nb^{DOF} = 35 412
		Fixed time step:
		$\Delta t = 10^{-3}$ s

Table 5: Simulation parameters for Stokes–Darcy flow with tows.

marized in Table 5, they are chosen to best reflect the real experimental conditions of the slurry cast process [2].

Figure 22b shows the evolution of the filter cake at different times for $\phi_s = 0.15$. It can be seen that the geometry fills correctly, while a particle-free region forms under the upper fiber. As mentioned previously, such particle-free zone can be found experimentally (Figure1). Therefore, the proposed numerical model also enables the prediction of the occurrence of such zones.

Moreover, while geometry certainly has an influence on the formation of macropores, it is interesting to examine the influence of initial suspension concentration on the formation of these particle-free regions. Figure 22 shows the evolution of the filter cake for two different initial concentrations. As can be observed, higher concentrations correlate with faster filling and a lower probability of macropore formation. This is supported by the volume flow rates plotted in Figure 23; the flow rate decreases more rapidly with increasing concentration for pressure-driven inlet conditions, corresponding to a faster pressure loss due to the faster cake growth. Globally, tows force the suspension to flow primarily along the left and right walls of the domain, resulting in the accumulation of cake on the lower-tow edge and then between both tows. It is in this intermediate region that concentration will drive the macropore formation (see Figure 21). Depending on the advancement velocity of the cake front (and thus the concentration), it may close under the upper tow, preventing particles from reaching the center and thereby allowing macropore formation. Consequently, the initial suspension concentration appears to exert a significant influence on the quality of the filling process.

The same study is now conducted for fluid-permeable and particle-impermeable tows. These tows are modelled as Darcy zones with an isotropic permeability (isotropy plane for unidirectional fibre tows) of 10^{-12} m^2 (Figure 24). While the fluid viscosity $\eta_f = 10^{-3}$ Pa.s is considered in the darcean tows (particles filtered), the viscosity of the slurry $\eta_s = 1.15 \times 10^{-3}$ Pa.s for $\phi_s = 0.1$ and $\eta_s = 1.25 \times 10^{-3}$ Pa.s for $\phi_s = 0.15$, determined from Eq. 2 is used for the Stokes flow, like for previous cases. The Level-Set zero iso-value is initialized around the tows, and its velocity is set to zero inside them to model impermeability to particles. The computation times here are

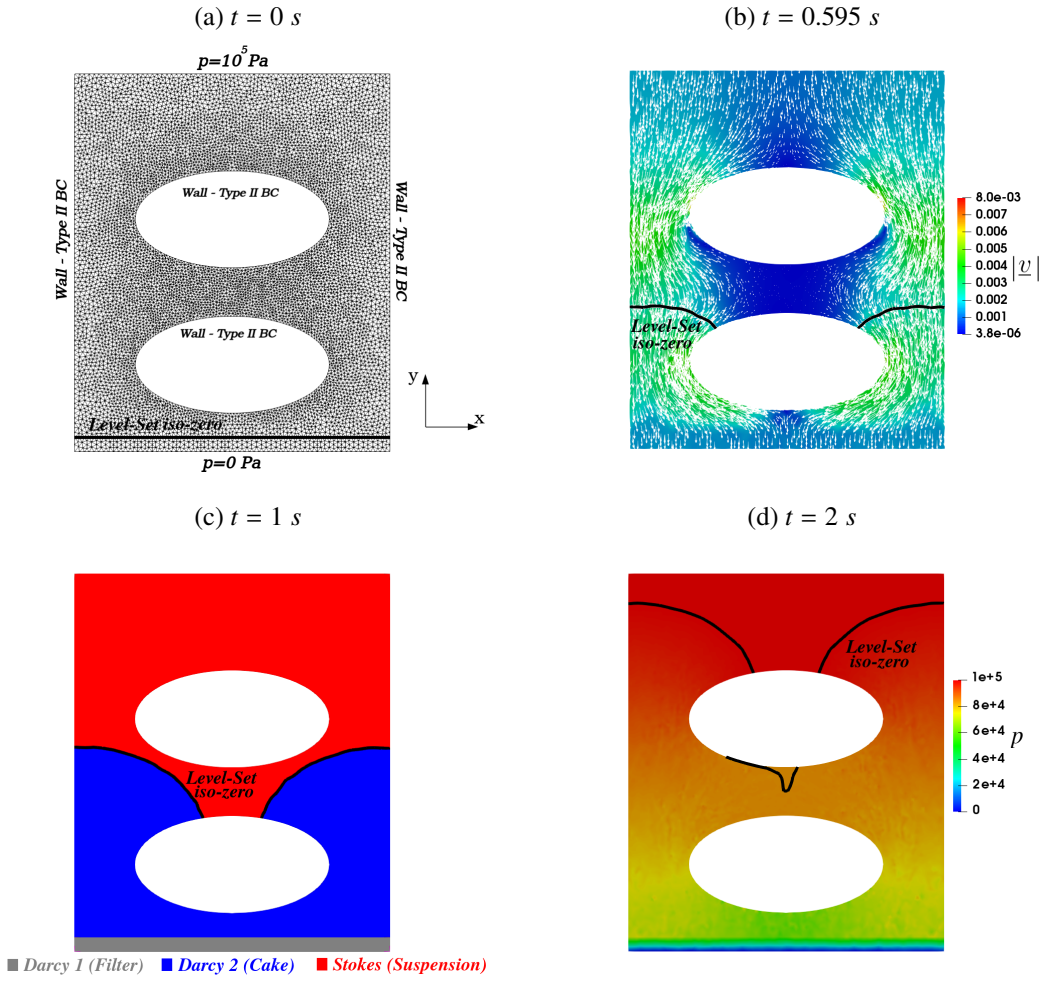

Figure 21: Pressure inlet controle injection for impermeable tows: temporal progression of the zero iso-value of the Level-Set function (black line). Additionally depicted are: (a) the mesh and boundary conditions, (b) representation of velocity field and magnitude, (c) delineation of physical zones, and (d) visualization of pressure field.

(a) $\phi_s = 0.1$

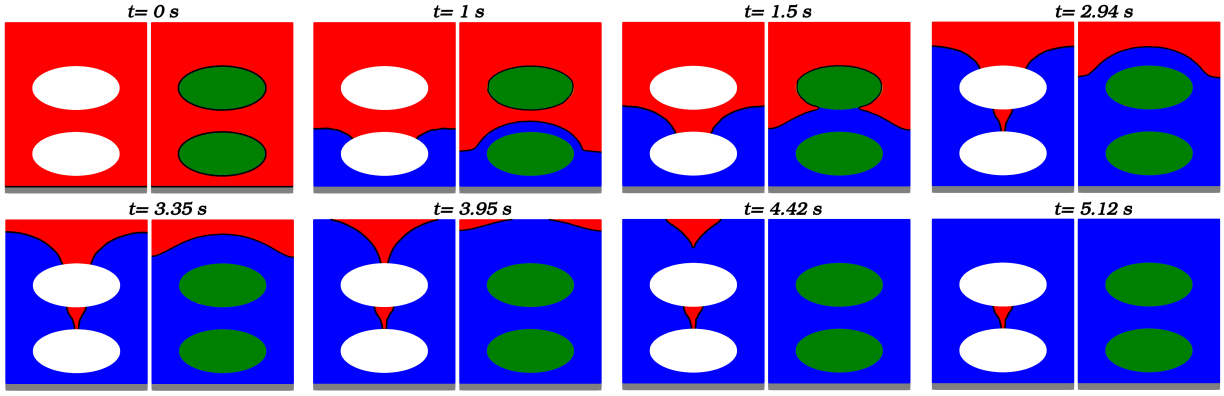

(b) $\phi_s = 0.15$

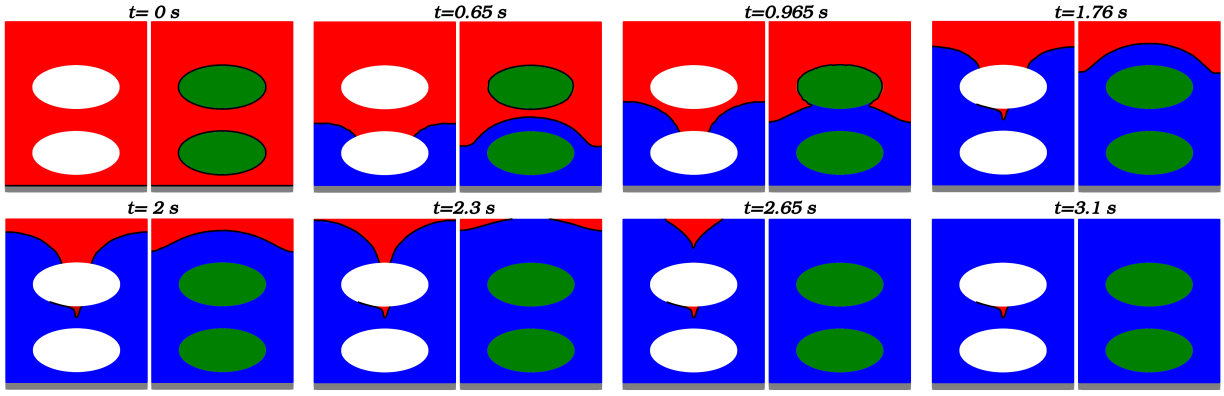

Figure 22: Filter cake evolution for different suspension concentrations: (a) $\phi_s = 0.1$, (b) $\phi_s = 0.15$. At each time: impermeable case on the left, permeable case on the right.

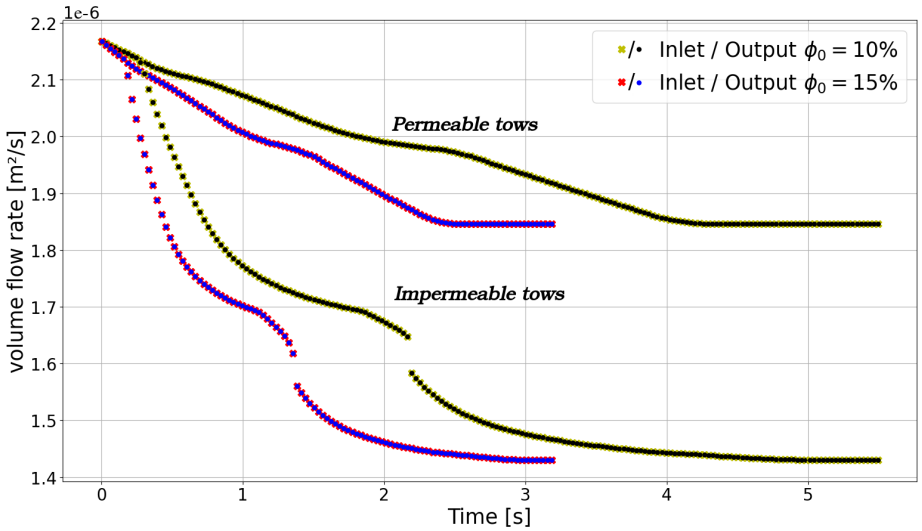

Figure 23: Comparison of volume flow rates at the inlet and outlet over time for the impermeable and permeable tow cases

approximately 2 hours ($\phi_s = 0.15$) and 3 hours 15 minutes ($\phi_s = 0.1$) for the impermeable case, and 3 hours ($\phi_s = 0.15$) and 5 hours 15 minutes ($\phi_s = 0.1$) for the permeable case. Figure 22 illustrates the displacement of the Level-Set iso-zero. It can be observed that, in this case, the filling occurs more rapidly than in the previous scenario with impermeable tows - compare Figures 21 and 24 -, and there is no macropore formation for both concentrations; although the increase in concentration also reduces the filling duration (see also Figure23). Similar to the previous case, the tows force the suspension to flow along the edges (Figure24). However, the permeability with respect to the fluid allows for a stronger flow towards the center, resulting in the formation of a cake above the tows. Consequently, when the cake front approaches the upper tow, the center is already filled, preventing the formation of macropores.

It would be relevant to study the influence of the various problem parameters on the formation of macropores. Particle-scale simulations (e.g. DEM) would certainly enable study of this phenomenon in greater details, including the influence of microscopic structure, whose influence is probably non-negligible. However, the present model at the industrial scale allows a focus on the influence of macroscopic data, such as geometric parameters, flow rate or initial suspension concentration. These in-depth investigations will contribute to a better understanding and optimization of the slurry cast process for manufacturing high-quality composite materials. These aspects are out of the scope of this model setting contribution, and will be examined in future work.

5. Conclusion

In this work was presented a numerical model of particle bed formation by suspension dead-end filtration. This modeling consists of a Stokes–Darcy coupling, with two porous possibly orthotropic domains involved for the region governed by Darcy with low permeabilities: the first being static (filter membrane), and the second changing with time (filter cake). As the particle

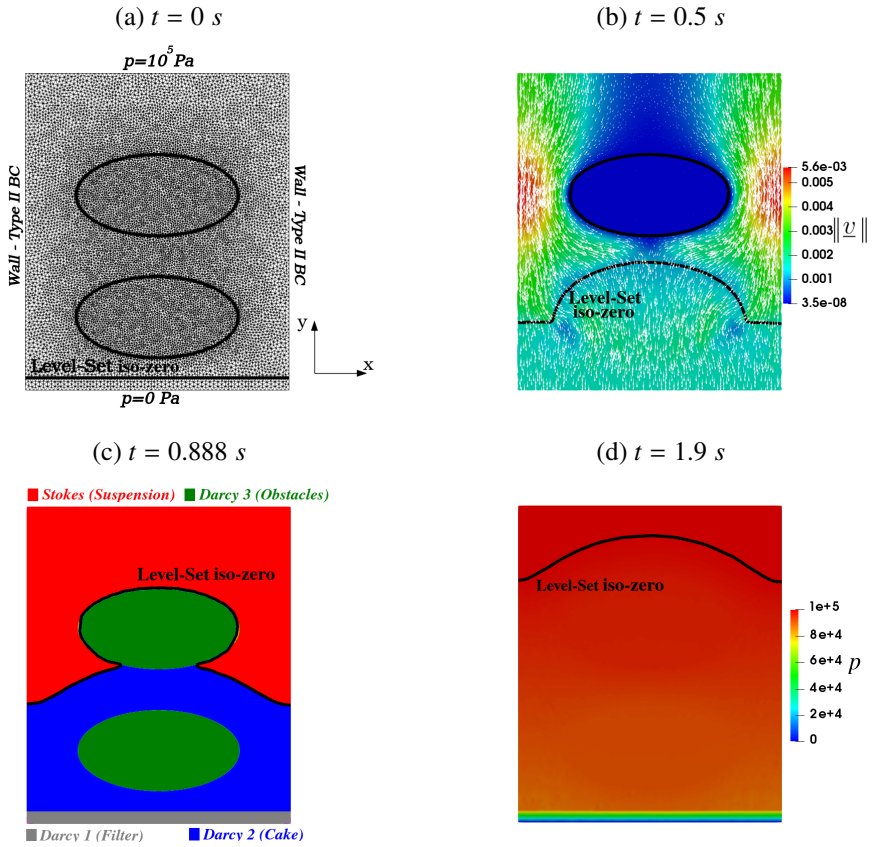

Figure 24: Pressure inlet controle injection for permeable tows: temporal progression of the zero iso-value of the Level-Set function (black line). Additionally depicted are: (a) the mesh and boundary conditions, (b) representation of velocity field and magnitude, (c) delineation of physical zones, and (d) visualization of pressure field.

concentration is low, the suspension can be considered as a Newtonian fluid and therefore solved by the classical Stokes' equations. The filter membrane and cake are modelled using Darcy's equations, with different isotropic permeabilities constant over time. The numerical solution of the problem is based on a monolithic approach using a single simplicial mesh. Discretization is performed using the P1/P1 velocity–pressure mixed finite element method, stabilized by the ASGS method. The moving interface separating the Stokes and Darcy zones is modelled using the Level-Set method. The displacement velocity of this interface is determined by a mass balance of the particles on across its surface. The transport equation of the Level-Set method is solved by a P1 finite element formulation stabilized by the SUPG method. The Stokes–Darcy and Level-Set problems are weakly coupled and solved on the same simplex mesh.

The results obtained were successfully validated by comparing numerical data with analytical solutions, including in 3D with anisotropic permeabilities, as well as by comparing them with existing experimental measurements [17]. This validation demonstrated that the present model offers an accurate representation of particle bed formation dynamics. Furthermore, solving the problem in the presence of tows enabled to model more complex cases, closer to industrial situations. The numerical results obtained were highly satisfactory: Level-Set displacement is accurate and particle-free zones, when they exist, can be described. However, the absence of relevant quantitative data in the literature makes it difficult to carry out a more in-depth analysis.

A number of research areas remain to be explored, including the influence of various parameters, such as initial suspension concentration, on the formation of particle-free zones. It would also be relevant to extend the model to other types of filtration, such as crossflow filtration, based for example on the Beavers–Joseph–Saffman condition [49, 50]. These are opportunities for future work aimed at improving our understanding of filtration phenomena and refining model parameters for even greater accuracy. Finally, this numerical approach has provided promising results for the modeling of suspension dead-end filtration, opening up opportunities for future research and contributing to the advancement of knowledge in this essential field for industry and other related applications.

References

[1] D. Lefevre, S. Comas-Cardona, C. Binetruy, P. Krawczak, Coupling filtration and flow during liquid composite molding: Experimental investigation and simulation, Composites Science and Technology 69 (13) (2009) 2127–2134.

[2] K. Dugois, Microscopic simulation and macroscopic analysis of impregnation process of composite material by a concentrated suspension, Ph.D. thesis, University of Bordeaux (2017).

[3] B. F. Ruth, G. H. Montillon, R. E. Montonna, Studies in filtration I. critical analysis of filtration theory, Industrial & Engineering Chemistry 25 (1) (1933) 76–82.

[4] B. F. Ruth, G. H. Montillon, R. E. Montanna, Studies in filtration, II. fundamental axiom of constant-pressure filtration, Industrial & Engineering Chemistry 25 (2) (1933) 153–161.

[5] B. F. Ruth, Studies in filtration III. derivation of general filtration equations, Industrial & Engineering Chemistry 27 (6) (1935) 708–723.

[6] F. M. Tiller, The role of porosity in filtration: I. numerical methods for constant rate and constant pressure filtration based on kozeny's law, Chemical Engineering Progress 49 (1953) 467–479.

[7] F. M. Tiller, The role of porosity in filtration: II. analytical equations for constant rate filtration, Chemical Engineering Progress 51 (1955).

[8] F. Tiller, The role of porosity in filtration: III. variable-pressure–variable-rate filtration, AIChE Journal 4 (2) (1958) 170–174.
[9] F. Tiller, C. Huang, Filtration equipment-theory, Industrial & Engineering Chemistry 53 (7) (1961) 529–537.
[10] M. Shirato, M. Sambuichi, H. Kato, T. Aragaki, Internal flow mechanism in filter cakes, AIChE Journal 15 (3) (1969) 405–409.
[11] F. M. Tiller, M. Shirato, A. Alciatore, Filtration in the chemical process industry, Matteson MJ, Orr C. Filtration: Principles and Practices, 2nd ed. New York: Marcel Dekker (1987) 361–474.
[12] K. Stamatakis, C. Tien, Cake formation and growth in cake filtration, Chemical Engineering Science 46 (8) (1991) 1917–1933.
[13] Y. Wu, An analysis of constant-pressure filtration, Chemical Engineering Science 49 (6) (1994) 831–836.
[14] P. B. Sørensen, P. Moldrup, J. Hansen, Filtration and expression of compressible cakes, Chemical Engineering Science 51 (6) (1996) 967–979.
[15] R. Wakeman, Thickening and filtration: A review and evaluation of recent research., Transactions of the Institution of Chemical Engineers 59 (3) (1981) 147 – 160.
[16] G. Belfort, R. H. Davis, A. L. Zydney, The behavior of suspensions and macromolecular solutions in crossflow microfiltration, Journal of Membrane Science 96 (1) (1994) 1–58.
[17] Y. J. Chew, W. Paterson, D. Wilson, Fluid dynamic gauging: A new tool to study deposition on porous surfaces, Journal of Membrane Science 296 (1-2) (2007) 29–41.
[18] P. C. Carman, Fluid flow through granular beds, Trans. Inst. Chem. Eng. London 15 (1937) 150–156.
[19] J. Olivier, J. Vaxelaire, E. Vorobiev, Modelling of cake filtration: an overview, Separation Science and Technology 42 (8) (2007) 1667–1700.
[20] A. Geoffre, N. Moulin, J. Bruchon, S. Drapier, Reappraisal of upscaling descriptors for transient two-phase flows in fibrous media, Transport in Porous Media 147 (2) (2023) 345–374.
[21] D. Smiles, A theory of constant pressure filtration, Chemical Engineering Science 25 (6) (1970) 985–996.
[22] D. Smiles, J. Kirby, Aspects off one-dimensional filtration, Separation Science and Technology 22 (5) (1987) 1405–1423.
[23] D. Smiles, Use of material coordinates in porous media solute and water flow, Chemical Engineering Journal 80 (1-3) (2000) 215–220.
[24] K. Atsumi, T. Akiyama, A study of cake filtration formulation as a stefan problem, Journal of Chemical Engineering of Japan 8 (6) (1975) 487–492.
[25] R. Wakeman, Numerical integration of the differential equations describing the formation of and flow in compressible filter cake, Trans. IChemE 56 (1978) 258–265.
[26] I. Tosun, Formulation of cake filtration, Chemical Engineering Science 41 (10) (1986) 2563 – 2568.
[27] M. S. Willis, I. Tosun, A rigorous cake filtration theory, Chemical Engineering Science 35 (12) (1980) 2427–2438.
[28] M. Willis, I. Tosun, W. Choo, G. Chase, F. Desai, A dispersed multiphase theory and its application to filtration, Advances in Porous Media 1 (1991) 179–294.
[29] G. G. Case, M. S. Willis, Compressive cake filtration, Chemical Engineering Science 47 (6) (1992) 1373–1381.
[30] R. Buscall, L. R. White, The consolidation of concentrated suspensions. Part 1: The theory of sedimentation, Journal of the Chemical Society, Faraday Transactions 1: Physical Chemistry in Condensed Phases 83 (3) (1987) 873–891.
[31] R. Bürger, F. Concha, K. H. Karlsen, Phenomenological model of filtration processes: 1. Cake formation and expression, Chemical Engineering Science 56 (15) (2001) 4537–4553.
[32] D. Lee, C. Wang, Theories of cake filtration and consolidation and implications to sludge dewatering, Water Research 34 (1) (2000) 1–20.
[33] K. Dong, R. Yang, R. Zou, A. Yu, G. Roach, E. Jamieson, Simulation of the cake formation and growth in sedimentation and filtration, in: Third International Conference on CFD in the Minerals and Process Industries, 2003, pp. 10–12.
[34] K. J. Dong, R. Zou, R. Yang, A. Yu, G. Roach, DEM simulation of cake formation in sedimentation and filtration, Minerals Engineering 22 (11) (2009) 921–930.
[35] H. P. Zhu, Z. Y. Zhou, R. Yang, A. Yu, Discrete particle simulation of particulate systems: theoretical develop-

ments, Chemical Engineering Science 62 (13) (2007) 3378–3396.
[36] H. Zhu, Z. Zhou, R. Yang, A. Yu, Discrete particle simulation of particulate systems: a review of major applications and findings, Chemical Engineering Science 63 (23) (2008) 5728–5770.
[37] Z. Zhou, S. Kuang, K. Chu, A. Yu, Discrete particle simulation of particle–fluid flow: model formulations and their applicability, Journal of Fluid Mechanics 661 (2010) 482–510.
[38] S. Sören, T. Jürgen, Simulation of a filtration process by DEM and CFD, International Journal of Mechanical Engineering and Mechatronics 1 (2) (2012) 28–35.
[39] R. Deshpande, S. Antonyuk, O. Iliev, Study of the filter cake formed due to the sedimentation of monodispersed and bidispersed particles using discrete element method–computational fluid dynamics simulations, AIChE Journal 65 (4) (2019) 1294–1303.
[40] V. Puderbach, K. Schmidt, S. Antonyuk, A coupled CFD-DEM model for resolved simulation of filter cake formation during solid-liquid separation, Processes 9 (5) (2021) 826.
[41] Y. Yap, F. Vargas, J. Chai, A Level-Set method for convective–diffusive particle deposition, Applied Mathematical Modelling 37 (7) (2013) 5245–5259.
[42] B. Goyeau, D. Lhuillier, D. Gobin, M. Velarde, Momentum transport at a fluid–porous interface, International Journal of Heat and Mass Transfer 46 (21) (2003) 4071–4081.
[43] H. Chen, X.-P. Wang, A one-domain approach for modeling and simulation of free fluid over a porous medium, Journal of Computational Physics 259 (2014) 650–671.
[44] D. Pino Muñoz, J. Bruchon, S. Drapier, F. Valdivieso, Sintering at Particle Scale: An Eulerian Computing Framework to Deal with Strong Topological and Material Discontinuities, Archives of Computational Methods in Engineering 21 (2) (2014) 141–187. doi:10.1007/s11831-014-9101-4.
URL https://hal-emse.ccsd.cnrs.fr/emse-01063698
[45] P. R. Nott, J. F. Brady, Pressure-driven flow of suspensions: simulation and theory, Journal of Fluid Mechanics 275 (1994) 157–199.
[46] J. F. Morris, F. Boulay, Curvilinear flows of noncolloidal suspensions: The role of normal stresses, Journal of Rheology 43 (5) (1999) 1213–1237.
[47] É. Guazzelli, O. Pouliquen, Rheology of dense granular suspensions, Journal of Fluid Mechanics 852 (2018) P1.
[48] A. Badia, Y. D'Angelo, F. Peters, L. Lobry, Frame-invariant modeling for non-brownian suspension flows, Journal of Non-Newtonian Fluid Mechanics 309 (2022) 104904.
[49] G. S. Beavers, D. D. Joseph, Boundary conditions at a naturally permeable wall, Journal of fluid mechanics 30 (1) (1967) 197–207.
[50] W. Jäger, A. Mikelić, On the roughness-induced effective boundary conditions for an incompressible viscous flow, Journal of Differential Equations 170 (1) (2001) 96–122.
[51] D. Nield, The Beavers–Joseph boundary condition and related matters: a historical and critical note, Transport in Porous Media 78 (2009) 537–540.
[52] E. Eggenweiler, Interface conditions for arbitrary flows in Stokes–Darcy systems: Derivation, analysis and validation, Ph.D. thesis, University of Stuttgart (2022).
[53] T. Carraro, C. Goll, A. Marciniak-Czochra, A. Mikelić, Effective interface conditions for the forced infiltration of a viscous fluid into a porous medium using homogenization, Computer Methods in Applied Mechanics and Engineering 292 (2015) 195–220.
[54] E. Eggenweiler, I. Rybak, Unsuitability of the Beavers–Joseph interface condition for filtration problems, Journal of Fluid Mechanics 892 (2020) A10.
[55] S. Osher, J. A. Sethian, Fronts propagating with curvature-dependent speed: Algorithms based on Hamilton–Jacobi formulations, Journal of Computational Physics 79 (1) (1988) 12–49.
[56] G. Pacquaut, J. Bruchon, N. Moulin, S. Drapier, Combining a Level-Set method and a mixed stabilized p1/p1 formulation for coupling Stokes–Darcy flows, International Journal for Numerical Methods in Fluids 69 (2) (2012) 459–480.
[57] L. Abouorm, M. Blais, N. Moulin, J. Bruchon, S. Drapier, A robust monolithic approach for resin infusion based process modelling, Key Engineering Materials 611 (2014) 306–315.
[58] R. Jackson, Locally averaged equations of motion for a mixture of identical spherical particles and a newtonian

fluid, Chemical Engineering Science 52 (15) (1997) 2457 – 2469, mathematical Modelling of Chemical and Biochemical Processes.
[59] J. Besson, R. Foerch, Large scale object-oriented finite element code design, Computer Methods in Applied Mechanics and Engineering 142 (1-2) (1997) 165–187.
[60] S. Badia, R. Codina, Unified stabilized finite element formulations for the Stokes and the Darcy problems, SIAM Journal on Numerical Analysis 47 (3) (2009) 1971–2000.
[61] L. Abouorm, R. Troian, S. Drapier, J. Bruchon, N. Moulin, Stokes–Darcy coupling in severe regimes using multiscale stabilisation for mixed finite elements: monolithic approach versus decoupled approach, European Journal of Computational Mechanics 23 (3-4) (2014) 113–137.
[62] M. Blais, N. Moulin, P.-J. Liotier, S. Drapier, Resin infusion-based processes simulation: coupled Stokes–Darcy flows in orthotropic preforms undergoing finite strain, International Journal of Material Forming 10 (2017) 43–54.
[63] P. Celle, S. Drapier, J.-M. Bergheau, Numerical modelling of liquid infusion into fibrous media undergoing compaction, European Journal of Mechanics-A/Solids 27 (4) (2008) 647–661.
[64] M. Discacciati, A. Quarteroni, S. Quinodoz, Numerical approximation of internal discontinuity interface problems, SIAM Journal on Scientific Computing 35 (5) (2013) A2341–A2369.
[65] P. Celle, Couplages fluide/milieu poreux en grandes déformations pour la modélisation des procédés d'élaboration par infusion, Ph.D. thesis, Ecole Nationale Supérieure des Mines de Saint-Etienne (2006).
[66] A. Dereims, S. Drapier, J.-M. Bergheau, P. De Luca, 3D robust iterative coupling of Stokes, Darcy and solid mechanics for low permeability media undergoing finite strains, Finite Elements in Analysis and Design 94 (2015) 1–15.
[67] L. Abou Orm, VMS (Variational MultiScale) stabilization for Stokes–Darcy coupled flows in porous media undergoing finite deformations: application to infusion-based composite processing., Ph.D. thesis, Ecole Nationale Supérieure des Mines de Saint-Etienne (2013).
[68] F. Brezzi, M. Fortin, Mixed and hybrid finite element methods, Vol. 15, New York: Springer-Verlag, 1991.
[69] A. N. Brooks, T. J. Hughes, Streamline upwind/Petrov–Galerkin formulations for convection dominated flows with particular emphasis on the incompressible Navier–Stokes equations, Computer Methods in Applied Mechanics and Engineering 32 (1-3) (1982) 199–259.
[70] M. Shakoor, B. Scholtes, P.-O. Bouchard, M. Bernacki, An efficient and parallel Level-Set reinitialization method–application to micromechanics and microstructural evolutions, Applied Mathematical Modelling 39 (23-24) (2015) 7291–7302.
[71] L. C. Ngo, H. G. Choi, Efficient direct re-initialization approach of a Level-Set method for unstructured meshes, Computers & Fluids 154 (2017) 167–183.
[72] A. Geoffre, Upscaling impregnation flows in random fibrous media application to infusion-based manufacturing process of composite materials, Ph.D. thesis, Ecole Nationale Supérieure des Mines de Saint-Etienne (2022).
[73] M. Sussman, P. Smereka, S. Osher, A Level-Set approach for computing solutions to incompressible two-phase flow, Journal of Computational physics 114 (1) (1994) 146–159.
[74] M. J. Rhodes, Introduction to particle technology, John Wiley & Sons, Ltd, 2008.
[75] P. B. Nedanov, S. G. Advani, A method to determine 3D permeability of fibrous reinforcements, Journal of Composite Materials 36 (2) (2002) 241–254.
[76] M. Blais, Modélisation et suivi du procédé par infusion de résine sur une nouvelle génération de renforts structuraux pour l'aéronautique, Ph.D. thesis, Ecole Nationale Supérieure des Mines de Saint-Etienne (2016).